# Review of aeronautical fatigue and structural integrity investigations in the UK during the period May 2021 - April 2023

Hallam David A

DSTL/TR150228 v1

21/06/2023

Dstl
Porton Down
Salisbury
Wiltshire
SP4 0JQ

## Release Conditions

This document has been compiled by Dstl but contains information released by each author's organisation for presentation to the International Committee on Aeronautical Fatigue and Structural Integrity (ICAF).

## Executive summary

This review is a summary of the aeronautical fatigue and structural integrity investigations carried out in the United Kingdom during the period May 2021 to April 2023. The review has been compiled for the 38th Conference and 31st Symposium of the International Committee on Aeronautical Fatigue and Structural Integrity (ICAF) on 26th – 29th June 2023 in Delft, The Netherlands and will be archived on the ICAF website https://www.icaf.aero/. Contributions generously provided by colleagues from within the aerospace industry and universities are gratefully acknowledged. The names of contributors and their affiliation are shown below the title of each item.

## Table of contents

# 1 Introduction

This review is a summary of the aeronautical fatigue and structural integrity investigations carried out in the United Kingdom during the period May 2021 to April 2023. The review has been compiled for the 38th Conference and 31st Symposium of the International Committee on Aeronautical Fatigue and Structural Integrity (ICAF) on 26th – 29th June 2023 in Delft, The Netherlands and will be archived on the ICAF website https://www.icaf.aero/.

The contributions generously provided by colleagues from within the aerospace industry and universities are gratefully acknowledged. The names of contributors and their affiliation are shown below the title of each item.

The format of the paper is similar to that of recent UK ICAF reviews; the topics covered include:

- Understanding fatigue behaviour
- Enhancing fatigue performance
- Developments in fatigue design tools
- Guidance and fatigue performance of additively manufactured parts
- Corrosion and fracture mechanics modelling technology
- Structural health and usage monitoring
- Advanced repair and coating technologies
- Advanced materials characterization technologies

References are annotated at the end of each contribution and are self-contained within the contribution.

# 2 Understanding Fatigue Behaviour

## 2.1 Overview and Comparison of Factors Controlling Fatigue Crack Initiation and Growth Processes at Varying Temperatures in Turbine Blade and Turbine Disc Ni Base Superalloys

*Philippa Reed, D. Kim, Y. Tan, D. Bull, Angelos Evangelou, Fabrice Pierron, Sari Octaviani, Somsubhro Chaudhuri, Nong Gao, Ian Sinclair, Andrew Hamilton, School of Engineering, University of Southampton, UK; Allan Harte, UKAEA, previously at University of Manchester; H. Toda, Kyushu University, Japan; Rong Jiang, Y. Zhao, College of Energy and Power Engineering, Nanjing University of Aeronautics and Astronautics, Nanjing 210016, China*

Crack initiation and early propagation behaviour of the directionally solidified (DS) superalloy CM247LC has been assessed by data rich imaging approaches. These include conventional characterization methods such as replica record analysis, 3D optical surface imaging, optical and scanning electron microscopy (SEM) as well as more recent techniques like digital image correlation (DIC) and synchrotron radiation computed tomography (SRCT). Three modes of secondary crack behaviours were found during evaluation of the fatigue process. The early stages of fatigue damage were controlled by microstructure-induced cracking, mainly consisting of carbide cracking. Fatigue damage was then promoted via slip band cracking and opening mode controlled carbide-cracking. The mechanisms of these different cracking behaviours are associated with the plastic zone of the main crack tip. Even though the early localized strain levels were of the same intensity within slip bands and at the intersection sites with carbides, carbide-induced cracking occurred prior to slip band cracking, characterized by SEM-DIC. This indicated that carbide-induced cracking was more likely to occur in the early stages of the fatigue process. Early crack growth behaviours were further investigated *in situ* at the microstructural scale via SRCT. The effect of carbides on crack initiation and propagation processes were evaluated in 3D. This revealed the phenomenon around pores, that cracks simultaneously grew on different slip planes in 3D, contrary to previous theories that such cracks tend to grow on a single favourable slip plane (in polycrystalline alloys). The SRCT result demonstrates the importance and necessity of 3D characterization of the crack propagation behaviour at sub-surface, which is not fully analyzed by 2D characterization.

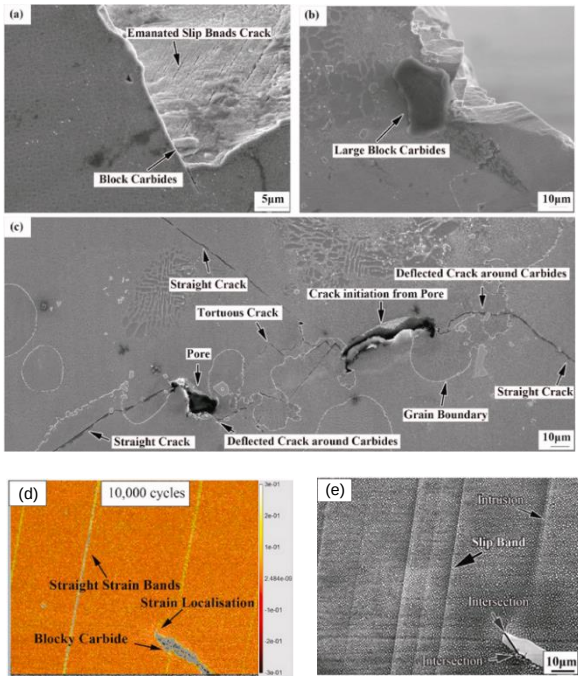


Figure 1 - (a) and (b) carbides at deflected parts of main crack; (c) propagation of a secondary crack (d) maximum shear stress distribution at interior of grain at 10,000 cycles determined by SEM-DIC; (e) SEM image of the carbide after 22,7000 cycles.

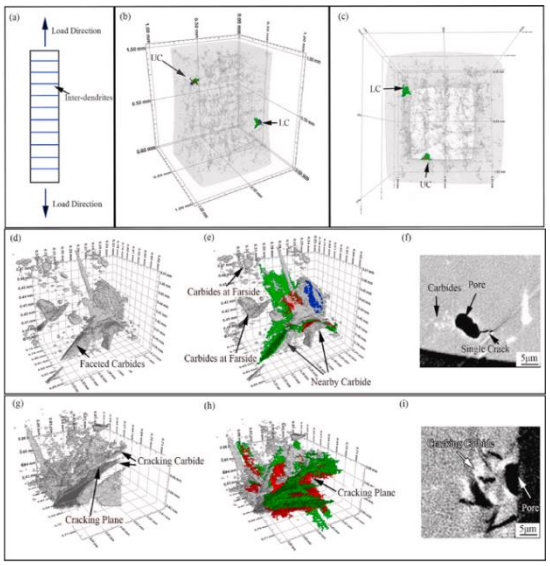


Figure 2 - (a) Schematic diagram of loading tension-tension test; (b) 3D rendering of the specimen in front view; (c) 3D rendering of the specimen in bottom; (d) carbides distribution around LC; (e) superimposed image of carbides and cracking planes around LC; (f) surface slice of LC; (g) carbides distribution around UC; (h) superimposed image of carbides and cracking planes around UC; (i) surface slice of UC.

More detailed discussion of these findings can be found in: “Data rich imaging approaches assessing fatigue crack initiation and early propagation in a DS superalloy at room temperature” by YG Tan, Daniel John Bull, Rong Jiang, Angelos Evangelou, Somsubhro Chaudhuri, Sari Octaviani, Fabrice Pierron, Nong Gao, H Toda, Ian Sinclair, PAS Reed (2021) Materials Science and Engineering: A, Volume 805, Pages 140592 https://doi.org/10.1016/j.msea.2020.140592

In another study on a turbine disc alloy at more elevated temperatures, the strain localisation under cyclic loading in an advanced powder metallurgy Ni-based superalloy (RR1000) at 450 °C was also characterised by SEM-DIC, and the related deformation substructures were characterised by electron channelling contrast imaging under controlled diffraction conditions (cECCI). The results indicate strain mainly accumulates in slip/strain bands due to dislocation slip on the {111} plane, and the strain saturates at 1000 cycles with no evident increase in strain value within strain bands or strain band density from 1000 cycles to 10,000 cycles. Analysis of the strain components in the local coordinates associated with each strain band shows the strain band mainly consists of shear strain $\epsilon_{xy}$ along the strain band and transverse strain $\epsilon_{yy}$ normal to the strain band. The strain bands can transmit through, be deflected, or be blocked at grain boundaries depending on the grain boundary characteristics and the neighbouring grain orientation. Comparing the strain bands obtained by SEM-DIC and deformation substructures obtained by cECCI shows that the strain bands originate from underlying continuous slip bands which show the sheared γ′ within the slip bands and dislocation pairs looping

around the γ′ precipitates, but the deformation localised in the discontinuous slip bands is not well characterised by SEM-DIC at this lateral resolution of strain.

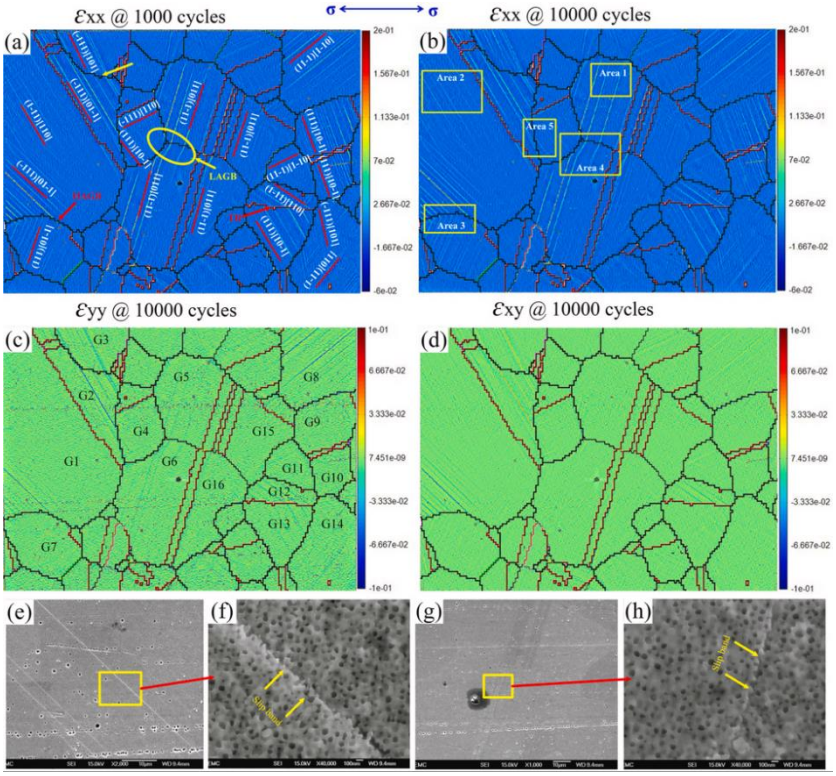


Figure 3 **-** (a) - ϵxx strain map at 1000 cycles; (b) ϵxx, (c) ϵyy and (d) ϵxy strain map at 10,000 cycles; (e)–(f) slip band morphology at 10,000 cycles.

More details can be found in: “Characterisation of strain localisation under cyclic loading at 450° C by SEM-DIC in a PM Ni-based superalloy” by Y Zhao, R Jiang, A Harte, DJ Bull, PAS Reed (2022) Materials Science and Engineering: A, Volume 849, Pages 143464 https://doi.org/10.1016/j.msea.2022.143464

Effects of microstructure and oxidation on fatigue crack initiation and early propagation processes were further investigated in the RR1000 turbine disc alloy which was studied with different γ′ distributions and carbide distributions on the grain boundary. Fatigue tests were carried out under three-point bending and trapezoidal waveform loading (with a 90 s dwell) at 650 °C in air. The failure mode in both γ′ variants is clearly characterised by intergranular features. A number of fatigue cracks are seen to initiate at grain boundaries with bulged Co-rich oxides at the surface and/or interfaces between carbides and grain boundaries, resulting from oxidation damage assisted by applied loading. Reduced lifetime is closely linked to significant intergranular crack initiation and frequent consequent crack coalescence events, which results in enhanced fatigue crack growth (FCG) rates. The extent of intergranular features and enhanced FCG are more marked where more continuous carbides exist at the grain boundary.

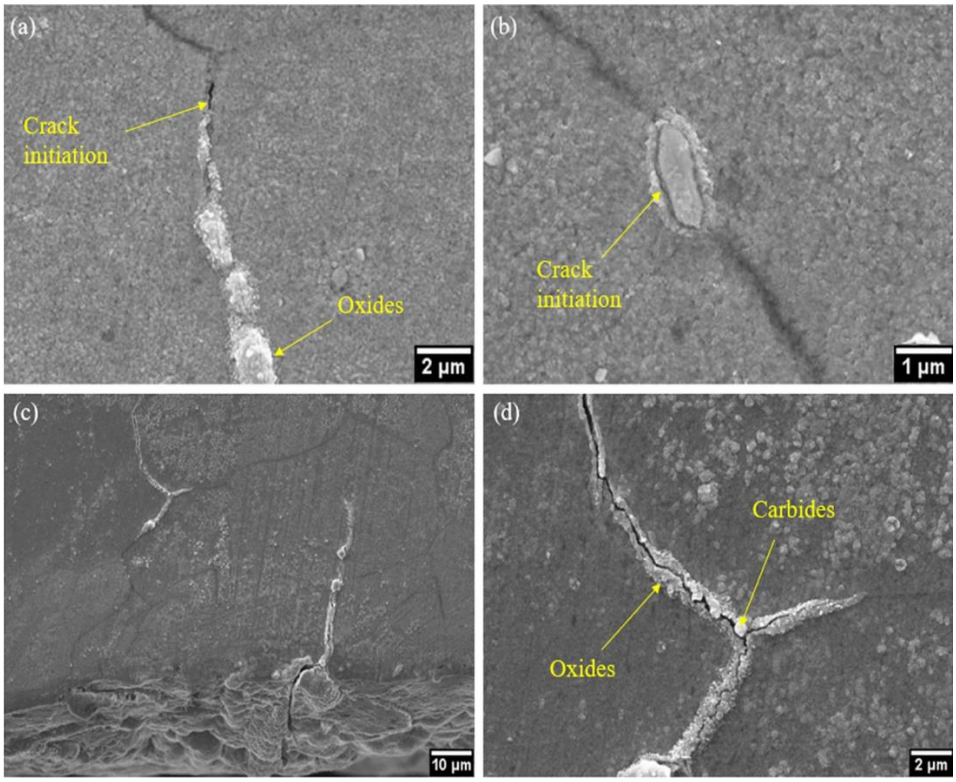


Figure 4 - SEI images of the coarse γ′ variant interrupted at 250 cycles (a) crack initiation along with oxide formed at grain boundary (b) crack initiation at the interface between carbide and grain boundary (c) grain boundary cracking through carbides and oxides formed at grain boundaries (d) image at higher magnification of image.

More details can be found in: “Microstructural and oxidation effects on fatigue crack initiation mechanisms in a turbine disc alloy” by D Kim, R Jiang, PAS Reed (2023) Journal of Materials Science, Pages 1-17 https://doi.org/10.1007/s10853-022-08120-9

As discussed in the previous study, two distinct and different unimodal γ' size distributions have been produced in a disc alloy RR1000 to understand the combined effects of γ' size (linked to slip character), grain boundary (GB) precipitates/carbides and dwell time on fatigue crack growth (FCG) mechanisms at elevated temperature. The FCG behaviour has been further investigated on single edge notched bend samples of both γ' variants at 650 °C under trapezoidal waveform loading with dwell times of 1 s and 90 s at maximum load. The fine γ' variant has better FCG resistance for both dwell times, and the difference in FCG rate becomes even more marked with longer dwell time. The coarse γ' variant exhibits faster and more time dependent FCG behaviour, with more evident intergranular fracture modes and rougher fracture surface than the fine γ' variant. Intergranular failure modes become dominant with the 90 s dwell time in both variants. A more continuous distribution of carbides is seen on the GB in the coarse γ' variant, which is likely to influence oxidation behaviour on GB and intergranular fracture behaviour. The effects of dwell time and consequent oxidation damage at the crack tip on fatigue behaviour are further investigated by transitioning between cyclic and time dependent regimes to assess the damage zones formed. The results show that an oxidation damage zone contributes to enhanced FCG after switching frequency from

cyclic to time dependent regimes while a tortuous crack path is related to crack wake (shielding due to prior crack path tortuosity), resulting in improved FCG resistance.

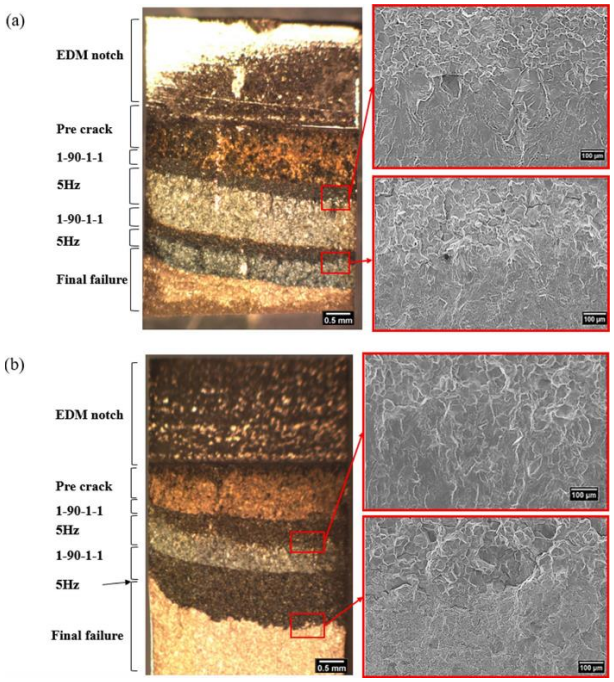


Figure 5 - Macroscopic images of half of the fracture surface showing the different regimes and associated SEM images of the two transitions of (a) fine γ′ variant and (b) coarse γ′ variant.

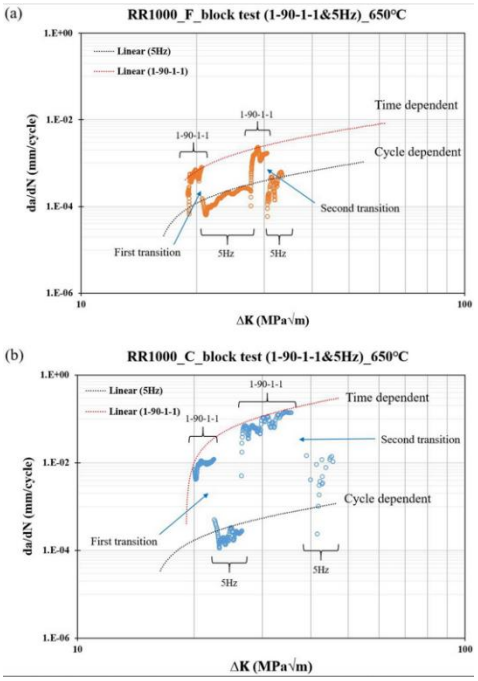


Figure 6 - FCG rates of block tests of (a) fine γ′ variant and (b) coarse γ′ variant.

More details can be found in: “Effects of γ' size and carbide distribution on fatigue crack growth mechanisms at 650° C in an advanced Ni-based superalloy” by D Kim, R Jiang, A Evangelou, I Sinclair, PAS Reed (2021) International Journal of Fatigue, Volume 145 https://doi.org/10.1016/j.ijfatigue.2020.106086

Understanding the mechanism of oxidation induced crack closure (OICC) is also of great importance in understanding the fatigue resistance of directionally solidified turbine blade materials operating at intermediate or high temperatures subjected to oxidation. Current work reveals that the occurrence of OICC is most closely related to the test frequencies and temperatures rather than the microstructure in the directionally solidified (DS) superalloy CM247LC. Characterization techniques in three dimensions - X-ray scanning tomography (CT) and two dimensions - scanning electron microscopy (SEM) with attached energy-dispersive X-ray spectroscopy (EDX) are combined to capture the oxides formed within the crack wake. These data are then incorporated into modified models to provide quantitative measurements of oxidation induced crack closure. Both the experimental and modelling results show that the external oxides forming close to the crack tip, result in a high crack tip opening displacement and thereby significant crack closure.

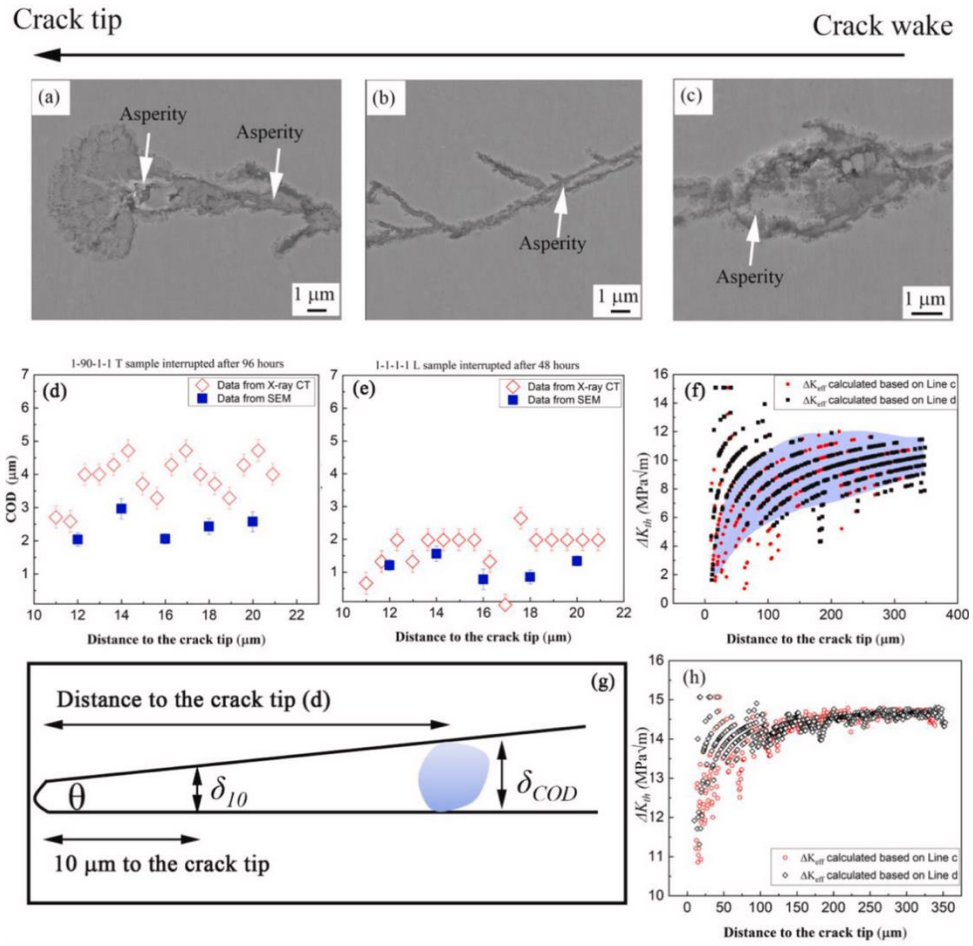


Figure 7 - The SEM images from the crack tip to the crack wake of the interrupted L sample, tested at 1-1-1-1 650 for 48 h: (a), (b), (c); COD measured by X-ray CT and SEM-EDX for the L, tested at 1-90-1-1, 650 for 96 h (d) and L, tested at 1-1-1-1, 650 for 96 h (e); $\Delta K_{eff}$ calculated based on Suresh's model (f); Schematic diagram of the model to estimate the CTOD (g); $\Delta K_{eff}$ calculated based on Louat's model (h).

More detailed discussion of these findings can be found in: "Oxidation induced crack closure in a nickel base superalloy: A novel phenomenon and mechanism assessed via combination of 2D and 3D characterization" by Yuanguo Tan, Nong Gao, Philippa Reed (2022) Materials Science and Engineering: A, Volume 861, Pages 144311 https://doi.org/10.1016/j.msea.2022.144311

Inconel 718 manufactured by Laser Powder Bed Fusion has also been characterized in terms of the microstructure, effect of post-processing heat treatment, and hence dependence of fatigue crack growth (FCG) on build orientation. Long crack fatigue tests were conducted at varying temperatures and frequencies. It was found that at 350 ºC (transgranular crack propagation) build orientation had no effect on FCG rates. However, at higher temperatures (time-dependent crack propagation) build orientation had a significant effect on FCG rates. This was primarily related to microstructural differences caused by the printing strategy in grain size distribution, grain shape and grain boundary character. Build orientation has a significant effect on high temperature fatigue crack propagation of additively manufactured parts even after post processing heat treatment. Vertical build specimens showed improved performance under time

dependent conditions. Crack arrest can occur with long dwells for vertical specimens caused by their specific microstructure.

More details can be found in: “Influence of build orientation on high temperature fatigue crack growth mechanisms in Inconel 718 fabricated by laser powder bed fusion: Effects of temperature and hold time” by D Martinez de Luca, AR Hamilton, PAS Reed (2023) International Journal of Fatigue, Volume 170, Pages 107484
https://doi.org/10.1016/j.ijfatigue.2022.107484

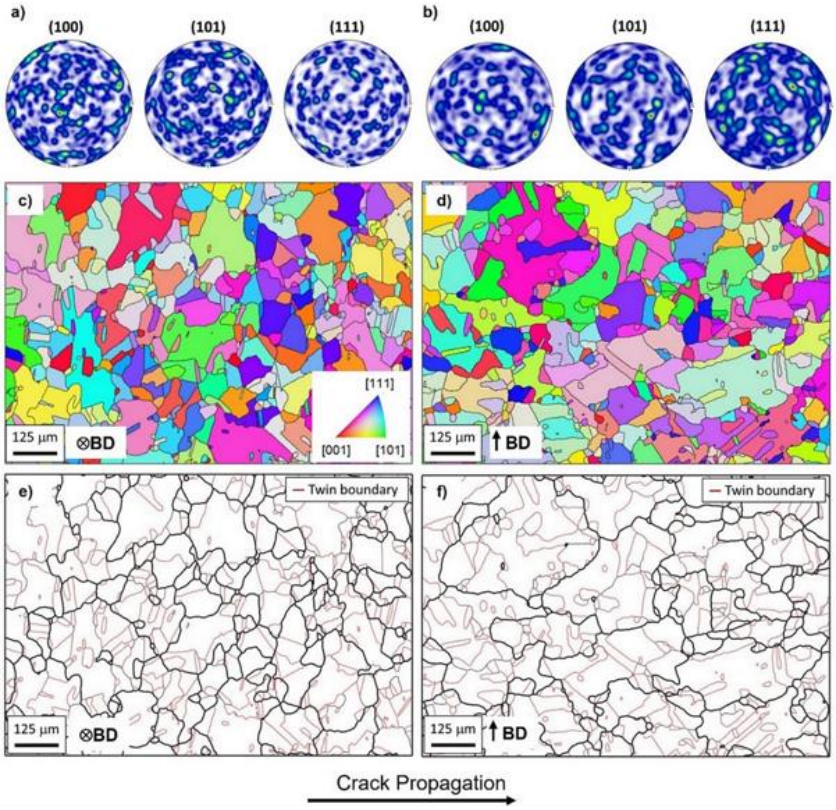


Figure 8 - EBSD micrographs of L-PBF IN718 microstructure (after post processing heat treatment). Pole figures for: a) vertical b) horizontal. Inverse pole figure maps for: c) vertical and d) horizontal. Twin grain boundaries for: e) vertical and f) horizontal.

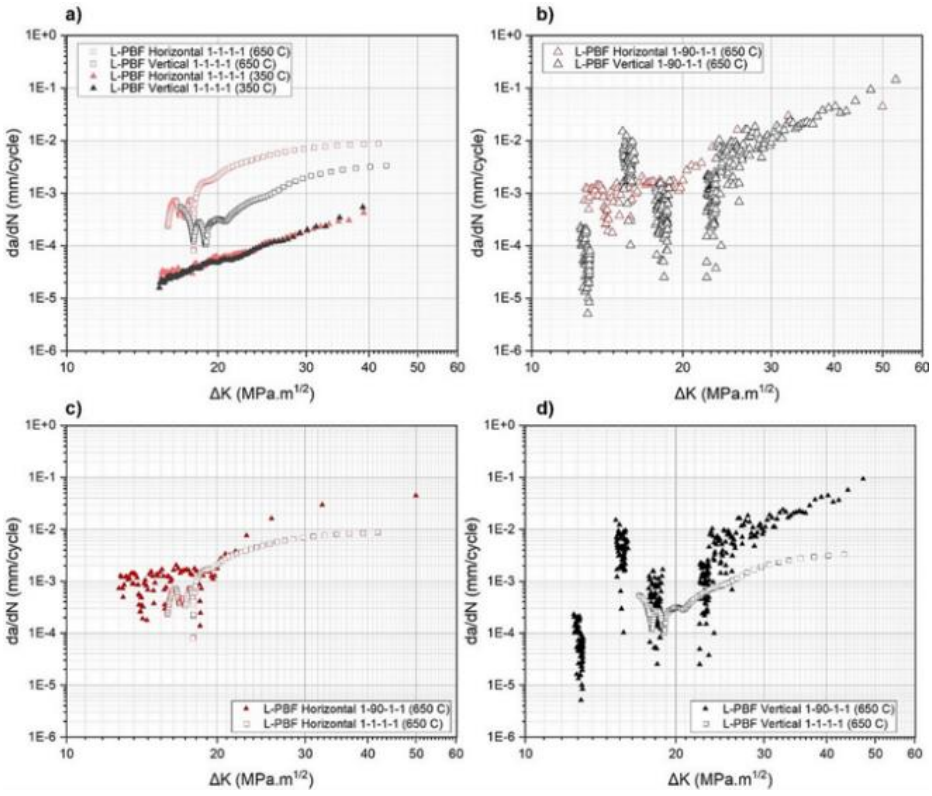


Figure 9 - FCG rates (da/dN vs ΔK) for both L-PBF orientations at 650 °C and different loading frequencies, comparison between: a) 1 s dwell tests, b) 90 s dwell tests, c) 90 s dwell and 1 s dwell for horizontal samples and d) for vertical samples.

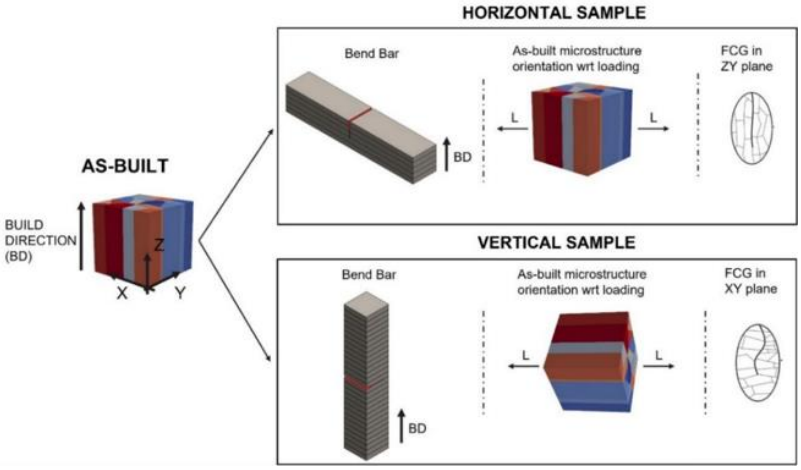


Figure 10 - Schematic of expected microstructure orientation (columnar grains in as-built configuration) with respect to loading direction.

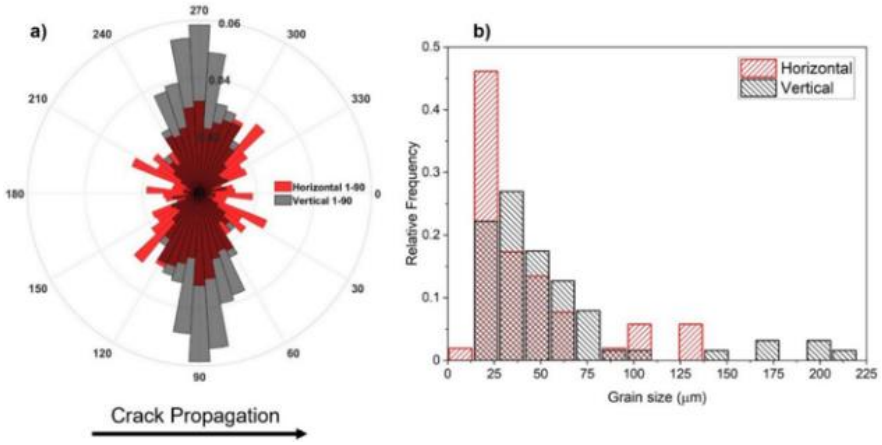


Figure 11 - Grain shape/size distribution for grains surrounding the main fatigue crack (testing at 650 ºC, and 1-90-1-1 frequency): a) weighted area histogram of grains long axis distribution (relative frequency) with respect to direction of crack propagation, b) grain size distribution.

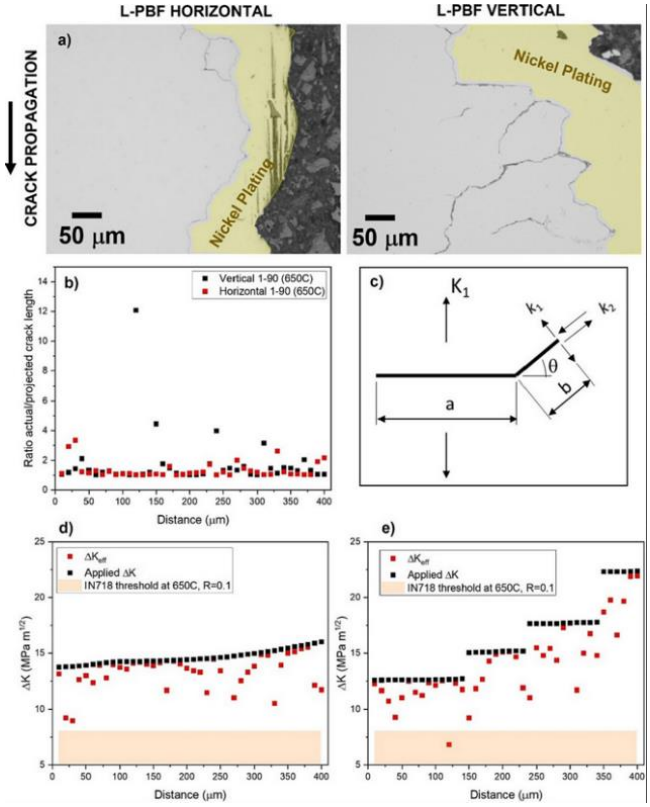


Figure 12 - Crack deflection measurements: a) Fracture surface sections showing deflected cracks for vertical and horizontal specimens b) ratio of actual/projected crack length vs distance c) Schematic of kinked crack and nomenclature for stress intensity factors d,e) ratio of ΔKeff / ΔK vs distance for horizontal (d) and vertical (e) specimens, (shading = IN718 literature threshold values).

# 3 Enhancing Fatigue Performance

## 3.1 Overview of Laser Shock Peening Effects in Airframe Material AA7075-T651 and the Benefits in Fatigue and Corrosion Mitigation

*Philippa Reed, Alvaro Sanchez, Julian Wharton, School of Engineering, University of Southampton, UK*
*Michael Fitzpatrick, Mitchell Leering, Faculty of Engng, Environment, and Computing, Coventry University, UK; Domenico Furfari, Airbus Operations GmBH, Germany; Daniel Glaser, CSIRO, South Africa; Chao You, College of Energy and Power Engineering, Nanjing University of Aeronautics and Astronautics, Nanjing 210016, China*

A laser shock peening (LSP) treatment was performed on AA7075-T651 for maximum fatigue improvement. Surface and microstructural characterisation techniques (micro-hardness, SEM-EBSD, contact-profilometry) showed LSP surface modification was limited, and LSP generated deep compressive residual stresses above −300 MPa. Fatigue testing showed a two-order magnitude increase in overall life, due to the mechanism of crack initiation changing from surface second-phase particles to subsurface crack initiation dependent on the local stress field. Modelling highlights the sensitive balance between surface roughness (including LSP-induced pits) and residual stress on the micro-mechanism of crack initiation, and how this can be used to maximise fatigue life extension.

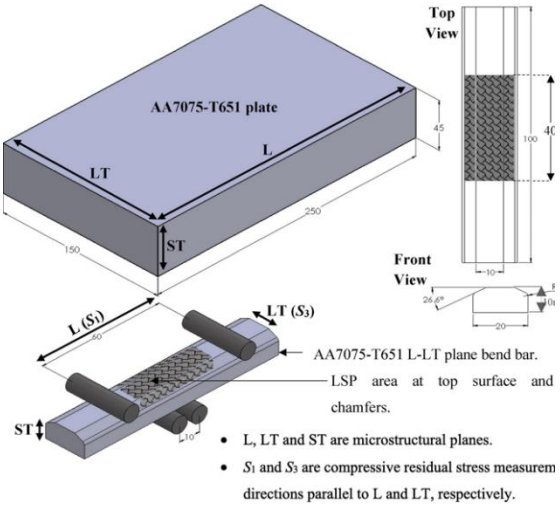


Figure 1 - Schematics of AA7075-T651 plate and LSP sample geometry and LSP area.

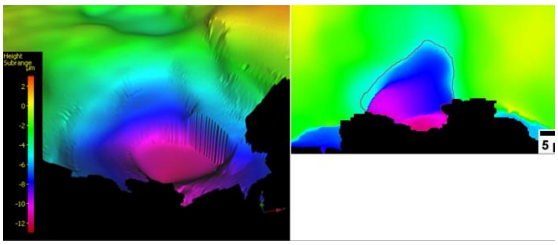

Figure 2 - Topographical images of both sides of pit acting as initiation site of LSP bend bar. Tested at 407 MPa stress range. Failed at 105 cycles. Taken from top surface (L-LT plane).

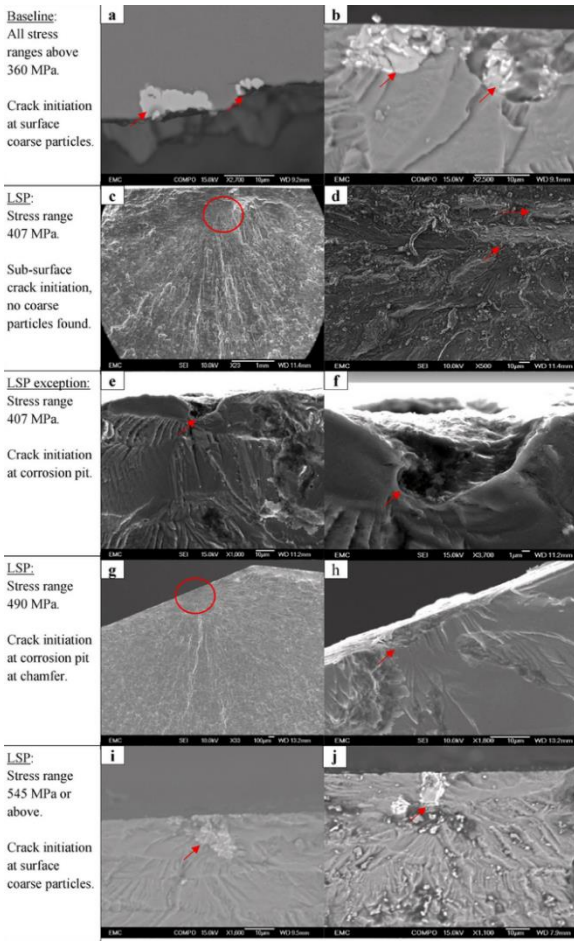


Figure 3 - Low and high magnification images of crack initiation sites for different fatigue test conditions. a-b: All baseline tests. c-d: LSP tests at 407 MPa stress range. e-f: One LSP test at 407 MPa which was an exception to the previous tests. g-h: LSP test at 490 MPa stress range. i-j: LSP tests at or above 545 MPa stress range.

More detailed discussion of these findings can be found in: “Effects of laser shock peening on the mechanisms of fatigue short crack initiation and propagation of AA7075-T651” by AG Sanchez, C You, M Leering, D Glaser, D Furfari, ME Fitzpatrick, JA Wharton, PAS Reed (2021) International Journal of Fatigue 143, 106025 https://doi.org/10.1016/j.ijfatigue.2020.106025

In a subsequent study the fatigue performance from pre-corroded pits was studied in laser-shock-peened AA7075-T651 with and without a protective ablation-layer. Surface and microstructural characterisation showed laser-shock-peening generated residual stresses up to −400MPa, limited hardness and moderate surface roughness increase. The laser-shock-peened specimens were exposed to 3.5 wt-% sodium chloride solution for different levels of galvanostatic control. The compressive residual stresses did not significantly affect corrosion behaviour, or corrosion pit morphology. Laser-shock-peening-induced surface roughness had the most detrimental impact on corrosion performance. Fatigue testing of pre-corroded AA7075-T651 showed pits act as stress

concentrations. Cracks initiated shortly after dynamic loading, reducing fatigue life by 50%. Laser-shock-peening increased fatigue life by 400% compared to corroded-untreated AA7075-T651, due to residual stresses effectively counteracting stress concentrations produced by pits.

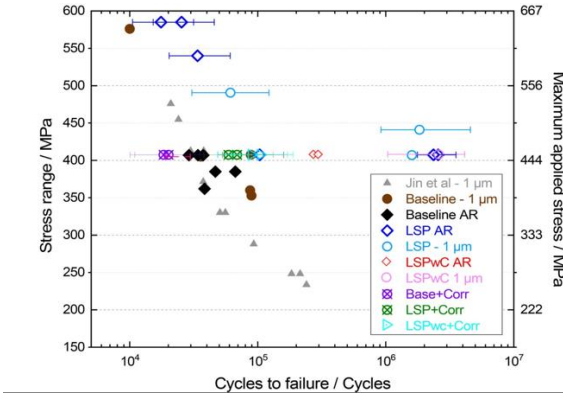


Figure 4 - Stress range vs. cycles to failure for AA7075 Type A (baseline), LSP and LSPwC samples (pre-corroded and uncorroded). Uncorroded baseline and LSP samples are taken from Sanchez et al.

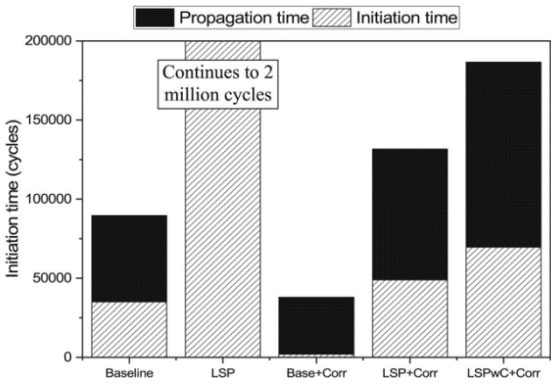


Figure 5 - Average initiation and propagation life of untreated AA7075 (baseline), LSP (LSPwC is expected to be the same), pre-corroded baseline, pre-corroded LSP and pre-corroded LSPwC. Columns show total fatigue life, including cycles at 0.1 and 0.5 load ratio.

More details can be found in: “Effects of ablative and non-ablative laser shock peening on AA7075-T651 corrosion and fatigue performance” by AG Sanchez, M Leering, D Glaser, D Furfari, ME Fitzpatrick, JA Wharton, PAS Reed (2021) Materials Science and Technology 37 (12), 1015-1034
https://doi.org/10.1080/02670836.2021.1972272

The effects of laser shock peening (LSP) on the fatigue life of AA7075-T651 were further investigated in a more detailed modelling approach. The combined influence of surface imperfections (i.e. pits and intermetallics), compressive residual stresses (CRS) and the applied stress on crack initiation sites (surface or subsurface) and the associated fatigue life were investigated. Critical surface imperfections were found to significantly reduce the benefits of LSP in life improvement, by promoting surface crack initiation despite the resisting effects of CRS. To facilitate quantifying the effects of LSP on fatigue life, a finite element (FE) model was developed to simulate residual stress distribution induced by LSP, as well as its redistribution caused by the formation of surface pits. Based on the FE results, a method identifying whether the specified surface pits and intermetallics are critical to lead to surface cracking at given stress conditions was proposed, based on the Smith-Watson-Topper method and the Murakami’s model respectively. The interaction between surface imperfections, CRS and the applied loads were taken into account in this method. In addition, a fatigue life assessment framework was proposed based on the prediction of crack initiation sites, which was validated to be reliable in efficiently evaluating the efficacy of the applied LSP in improving fatigue life.

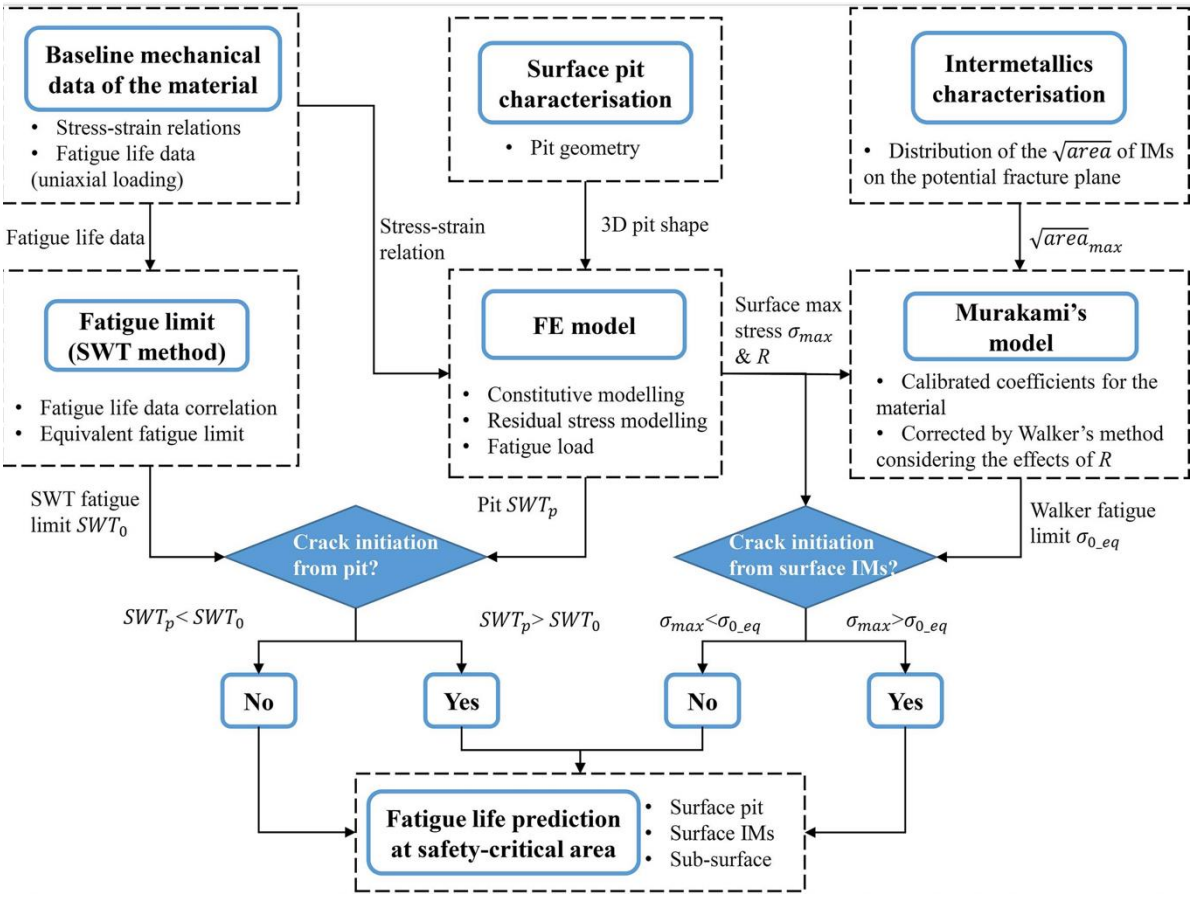


Figure 6 - Framework of fatigue life assessment based on the prediction of crack initiation sites.

More details can be found in: "The effects of surface pits and intermetallics on the competing failure modes in laser shock peened AA7075-T651: Experiments and modelling" by C You, AG Sanchez, M Leering, D Glaser, D Furfari, ME Fitzpatrick, JA Wharton, PAS Reed (2022) International Journal of Fatigue 155, 106568 https://doi.org/10.1016/j.ijfatigue.2021.106568

# 4 Developments in Fatigue Design Tools

## 4.1 General Developments in Fatigue Analysis

*A. Halfpenny and R Plaskitt, Hottinger Bruel & Kjaer Ltd, United Kingdom*

HBK continue to develop their material fatigue testing capabilities and the fatigue damage models used in their nCode software products for fatigue and durability analysis.

- nCode DesignLife, for fatigue analysis from finite element analysis stress results, has been developed to support:
  - Extension of “Dang Van” high cycle multiaxial fatigue damage model to support multi-isothermal temperature analyses.
  - Fatigue damage models for adhesive bonds.

- The Advanced Materials Characterisation & Test laboratory (AMCT) has completed some relevant and publicly presented fatigue testing:
  - Strain-controlled fatigue testing to characterise surface treatment effects in landing gear materials. See summary of ICAF 2023 paper below.
  - Strain-controlled fatigue tests on additively manufactured titanium Ti-6Al-4V alloy, manufactured by wire-arc directed energy deposition (WA-DED). See abstract of ICAF 2023 paper below.
  - Strain-controlled fatigue tests on additively manufactured titanium Ti-6Al-4V alloy, Inconel 718 and Aluminium AlSi10Mg, manufactured by laser beam powder bed fusion (LB-PBF). The fatigue performance of each material was assessed including one or more of the following different heat treatment, build layer orientation and/or powder storage and recycling scenarios. This research is nearing completion and is in collaboration with TWI Technology Centre (Yorkshire, UK), fatigue testing is complete, fatigue characterisation and reporting are in progress.

## 4.2 Tools and Methods for Landing Gear Fatigue Analysis with Surface Treatment Effects

*R. Plaskitt[1], M. Hill[1], A. Halfpenny[1], B. Griffiths[2], A Clark[3], B. Madsen[4]*

*[1] Hottinger Bruel & Kjaer Ltd, United Kingdom, rob.plaskitt@hbkworld.com*

*[2] Select Engineering Services, USA*

*[3] USAF Landing Gear Systems, USA*

*[4] General Atomics Systems Integration, USA*

Early work was reported at ASIP 2019 and in the 2021 UK National Review, further work is reported by oral presentation and proceedings of ICAF 2023. The following are extracted to summarise the paper.

Table 1 shows the material and surface treatment combinations fatigue tested and characterised. Figure 1 (a) shows Coffin-Manson-Basquin strain-life curves for 300M steel (polished baseline) and with electrolytic nickel plating surface treatment. This shows the surface treatment has a very significant detrimental effect on high cycle

fatigue, and (b) shows an equivalent collapsed view of these strain-life curves. The purpose of this collapsed view is for better visual comparison of the goodness of fit of the $K_{sur}$ curve for validation of the $K_{sur}$ surface treatment factor characterisation method applied to strain-life curves. In this case, rather than fitting a $K_{sur}$ curve through the measured data points, the data points are rotationally transformed by $K_{sur}$ to ideally overlay the polished data points. This collapsed view also allows a comparison of the relative design curves.

Table 1: Material and surface treatment combinations tested.

| Material | Surface Treatment |
|---|---|
| 300M steel | Polished , without shot peen (***baseline***), with shot peen. |
| | Electrolytic nickel coating (plated to size, ground to size), with and without shot peen. |
| | Electroless nickel coating (plated to size), with and without shot peen. |
| | Cadmium coating, with and without shot peen. (*always plated to size, never ground*) |
| | Chrome coating (plated to size, ground to size), with and without shot peen. |
| | Chrome coating (plated to size, ground to size), shot peen, strip & replate six times. |
| 4340 steel | Polished, without shot peen (***baseline***). |
| | Chrome coating (ground to size), with and without shot peen. |
| | Chrome coating (ground to size), shot peen, strip & replate six times. |
| 7075 aluminium | Polished, without shot peen (***baseline***). |
| | Anodised, with and without shot peen. |

(a) Strain-life curves for baseline and surface treatment.

(b) Strain-life curves for baseline and *collapsed* surface treatment.

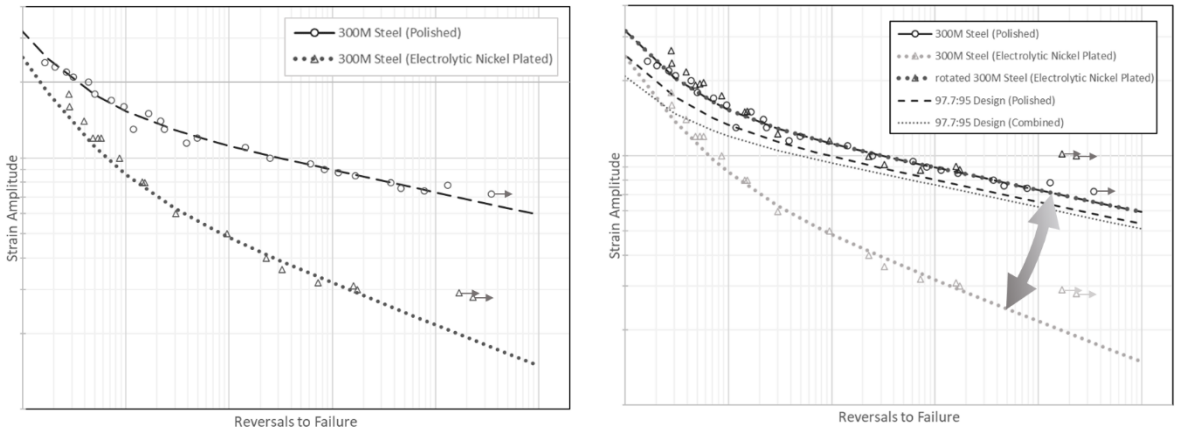


Figure 1 - (a) The Coffin-Manson-Basquin strain-life curves for polished baseline and surface treatment, and (b) with an equivalent collapsed view of the surface treatment strain-life curve.

Results for other materials and surface treatment coating and process combinations have shown varying levels of $K_{sur}$ surface treatment factors, some that are detrimental to fatigue performance, some that have negligible effect, and some that are beneficial to fatigue performance. In all cases other than electrolytic nickel, the shot peening process was very effective in restoring the negative effect of the tested coatings.

Different surface treatments can have a detrimental or beneficial effect on high cycle fatigue. For the material and surface treatment combinations tested and listed in Table 1, these fatigue tests and subsequent characterisation have quantified these surface treatment effects. They have shown that the surface treatment factor, $K_{sur}$ method, can be successfully applied with the strain-life fatigue method with an acceptable fit to the measured data. This validates the decision enabling the reduction in fatigue test sample size enabling more efficient testing, i.e., more surface treatments quantified within the same budget or total number of tests. Furthermore, the surface treatment factor, $K_{sur}$ model, can be used in statistical analyses to represent a combined material and surface treatment design curve with a specified reliability and confidence.

Fatigue test results have led to the following conclusions that are specifically relevant to selected materials and surface treatment conditions:

1. Chrome plating of steel (or anodizing of aluminium) has a significant and adverse effect on the high-cycle fatigue performance of the material. However, its effect on low-cycle fatigue performance is much less. The $K_{sur}$ method shows good correlation with the observed results.
2. Shot peening prior to chrome plating (or anodizing) appears to negate completely the detrimental effects of the process.
3. Repetitive surface treatment applications appear to contribute to the statistical scatter, but do not adversely affect the mean fatigue behaviour.

Fatigue testing work is continuing to consider more materials, more surface treatments, coating depths, the effect of re-applications, etc. However, the results are revealing that surface treatment $K_{sur}$ factors are often transferable between similar materials with similar surface treatments. Used correctly, the surface treatment $K_{sur}$ factors can be combined to investigate the effects of multiple surface treatments. This allows useful design insights to be made before a specific surface treatment combination and overhaul repetition is tested.

# 5 Guidance and Fatigue Performance of Additively Manufactured Parts

## 5.1 Guidance on the Qualification and Certification of Additive Manufactured Parts for Military Aviation - MASAAG Paper 124 Issue 2

*D. Fletcher, Defence Science and Technology Laboratory (Dstl)*

Military Aircraft Structural Airworthiness Advisory Group (MASAAG) paper 124 is designed to act as a guidance document that brings together Military Airworthiness Authority (MAA) airworthiness regulations / standards and Additive Manufacturing (AM) literature with the goal of supporting the MAA, the Type Airworthiness Authority (TAA) and Design Organisations (DO) to qualify and certify an AM part as airworthy.
Issue 2 [1] has now been released with the addition of:

- Chapter 5: airworthiness assurance for manufactured parts for use in aircraft systems
- Chapter 7: part design and build for polymer additive manufacturing

### 5.1.1 Issue 2 Additions:

#### 5.1.1.1 Chapter 5:

Chapter 5 is designed to guide the reader through the regulations and certification standards that are used for the airworthiness assurance of manufactured components for aircraft systems. Focus is placed on the design, manufacture, qualification and certification of structural components contained within any aircraft system that may affect the airworthiness of a type 1 military aircraft (high manoeuvrability combat air systems). In addition to type 1 military aircraft the chapter is also relevant to other military operated aircraft covered by parallel regulations / standards, with the exception of rotorcraft mechanical systems.

#### 5.1.1.2 Chapter 7:

Chapter 7 is designed to provide a guide for those involved in the design or redesign of a component to be produced using polymer AM with a focus on Fused Deposition Modelling and Laser Powder Bed Fusion. The importance of process variables is discussed alongside guidance on how they might be controlled or measured. The need to supply a process control document (PCD) alongside airworthiness documentation is also emphasised, as is the need for changes in the PCD to be subject to the Military Certification Review Item (MCRI) process.

### 5.1.2 Proportionate Qualification and Certification Guidance

Following the publication of MASAAG paper 124 issue 2 the requirement for tiered qualification and certification guidance, which can be applied over a range of safety criticality levels, has been identified. Focus is now being placed on addressing this challenge of proportionality through industry, government and international engagement to inform the creation of new guidance documentation.

### References

1. https://assets.publishing.service.gov.uk/government/uploads/system/uploads/attachment_data/file/1120270/MASAAG_Paper_124.pdf

## 5.2 Influence of As-Deposited Surface Condition on the Fatigue Strength of Titanium Alloy Ti-6Al-4V Built By Wire-DED Additive Manufacturing

*Xiang Zhang, Muhammad Shamir, Abdul Khadar Syed, Wayne Sadler*
*Coventry University, Centre for Manufacturing and Materials*

Wire-arc directed energy deposition (wire-DED), also known as wire-arc additive manufacturing (WAAM) is a metal 3D printing technique that is recognised for its high efficiency and cost-effectiveness (short lead time and 100% usage of the feedstock materials), flexibility in large-scale builds and suitability for the aerospace, energy, and construction sectors. Surface waviness or undulations in the as-deposited condition cause stress concentration which can cause premature crack initiation under fatigue loads. However, machining and polishing add another process, which may not be necessary for parts that are subjected to relatively lower operational loads.

The work reported here is a part of the New Wire Additive Manufacturing (NEWAM) research programme funded by the UK Engineering and Physical Science Research Council (EPSRC, Grant No. EP/R027218/1)[1,2]. The key findings are summarised as follows.

In the experimental work, specimens were extracted from a WAAM “Wall” shown in Fig. 1. Local stress concentration at the troughs of surface undulations was quantified by a contact type metrology tool in conjunction with finite element stress analysis; the stress concentration factors ranged between 1.25-1.85 for the Ti-6Al-4V build (Fig. 2). Fatigue test was conducted under bending load with cyclic load ratio 0.1 (Fig. 3). The S-N data (Fig. 4) shows that (i) fatigue strength was reduced considerably at a given life comparing with specimens with machined and polished surfaces; the worst case being 50% reduction in strength at 300,000 load cycles; (ii) fatigue life decreased significantly under the same applied stress, e.g., 10 times reduction in life at applied bending stress 600 MPa.

The applicability of two predictive methods was studied. The traditional notch-stress method does not give a consistent prediction capability; using the deepest trough ($K_t$=1.85) it predicted well for the lower stress tests, while using the shallowest trough ($K_t$=1.25) the prediction was much better for the higher stress tests (Fig. 5). The poor agreement with the test is attributed to the early crack initiation from the troughs and the crack propagation phase being dominant, i.e., the mechanism is not crack initiation. The fracture mechanics approach has delivered good and consistent predictions at every applied stress level (Fig. 6). The method treats a trough as an initial crack, and the depth of a trough as an equivalent initial flaw size (EIFS). In this WAAM Ti64 material, EIFS value range of 0.05-0.32 mm covered the range of measured trough depths. This approach is shown to be suitable for predicting the fatigue life of the WAAM built titanium alloy in as-deposited surface condition.

Details of this work can be found in our recent paper [3].

## References

[1] “New Wire Additive Manufacturing (NEWAM)”, UK Engineering and Physical Sciences Research Council (EPSRC), https://gow.epsrc.ukri.org/NGBOViewGrant.aspx?GrantRef=EP/R027218/1.

[2] “New Wire Additive Manufacturing (NEWAM)”, UK Research and Innovation (UKRI), https://gtr.ukri.org/projects?ref=EP%2fR027218%2f1.

[3] Muhammad Shamir, Xiang Zhang, Abdul Khadar Syed, Wayne Sadler. Predicting the effect of surface waviness on fatigue life of a wire + arc additive manufactured Ti-6Al-4V alloy, *materials*, submitted 26/5/2023 [Preprints available at www.preprints.org doi:10.20944/preprints202305.2188.v1]

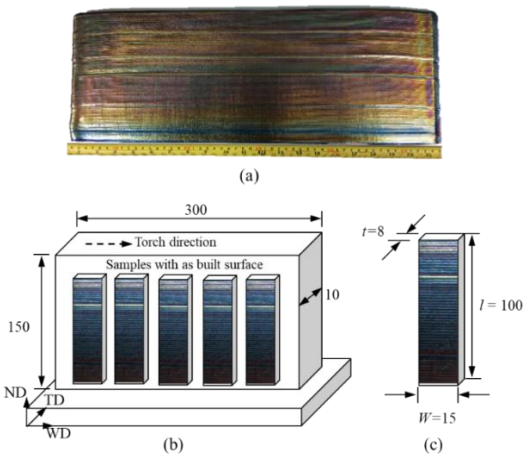


Figure 1 - (a) WAAM Ti64 wall by single-pass deposition, (b) sample extraction, (c) as-built specimens [WD = weld torch movement direction, TD = transverse direction, ND = normal direction].

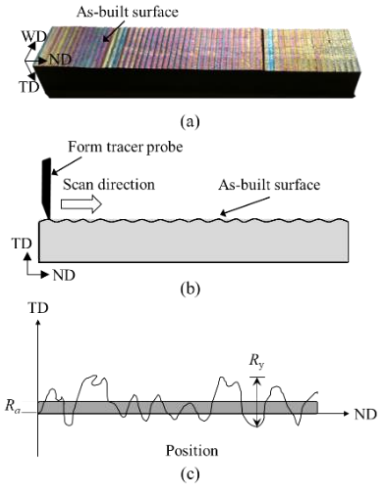


Figure 2 - (a) fatigue samples with as-deposited surface waviness, schematic of (b) as-deposited surface waviness, (c) surface waviness parameters.

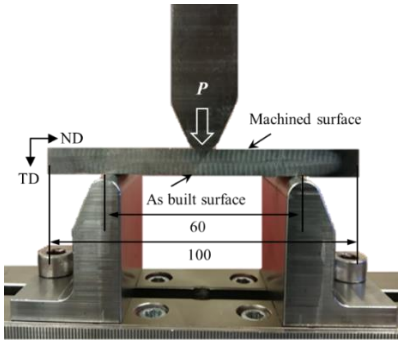


Figure 3 - set-up of 3-point bending fatigue test; the as-deposited surface faced downwards, under tensile fatigue stresses (unit: mm).

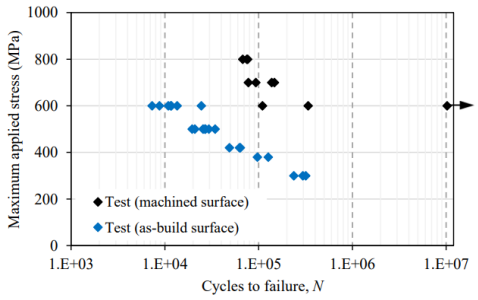


Figure 4 - S-N data for machined and as-deposited samples. The y-axis is the maximum bending stress on the beam lower surface at the mid-span.

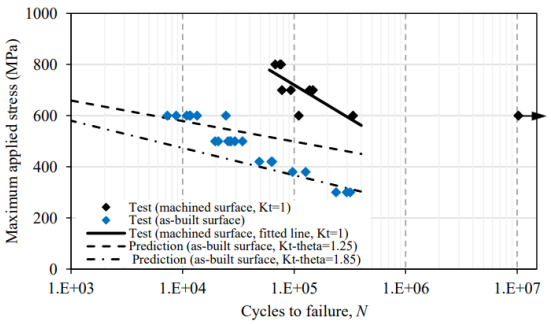


Figure 5 - Predicted S-N curves for specimens with surface waviness by the notch stress approach.

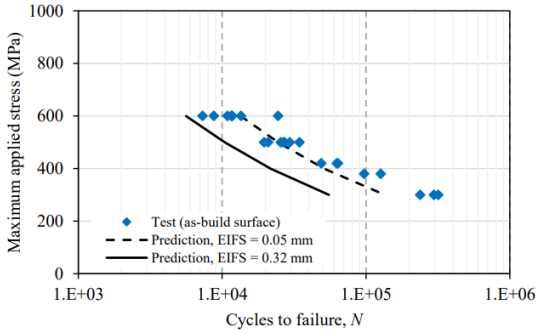


Figure 6 - Predicted S-N curves by fracture mechanics using two EIFS values representing the lower and upper values of surface troughs.

## 5.3 Fatigue Performance and Cyclic Deformation Behaviour of Titanium Alloy Ti-6Al-4V by Wire+Arc Additive Manufacturing

*R. Plaskitt[1], M. Hill[1], A. K. Syed[2], X. Zhang[2]*

*[1] Hottinger Bruel & Kjaer Ltd, United Kingdom, rob.plaskitt@hbkworld.com*

*[2] Coventry University, UK*

Previous work was reported by HBK and Coventry University in the 2021 UK National Review. This summarises further work on the fatigue behaviour of titanium alloy Ti-6Al-4V manufactured by Wire+Arc Additive Manufacturing (WAAM), as submitted to ICAF 2023 for poster presentation and proceedings. The following are extracted to summarise the paper.

NEWAM (NEw Wire Additive Manufacturing) is a 6 year research programme (2018 to 2024) focused on the process, material and structural integrity of wire based directed energy deposition (DED) additive manufacture (AM) processes. Four UK universities (Cranfield, Manchester, Strathclyde and Coventry) are combined in this research programme with UK EPSRC funding and industry support. Project partners include aerospace OEMs who are interested in the future potential of this manufacturing method for increased material buy-to-fly ratio, manufacturing lead time reduction and weight reduction.

The paper describes the fatigue performance and cyclic deformation behaviour of as-built WAAM titanium Ti-6Al-4V alloy. Two WAAM walls were manufactured with an oscillatory torch and wire path. Test samples were extracted from these walls and prepared for microstructure analysis, tensile and fatigue tests. Microstructure analysis included scanning electron microscope (SEM), electron back scatter diffraction (EBSD) and micro X-ray computed tomography (micro-XCT). Tensile and fatigue tests were conducted on samples extracted in parallel with the deposition layers (horizontal orientation in the wall) and perpendicular to the deposition layers (vertical orientation). Fatigue tests were strain controlled at room temperature with fully reversed (strain ratio

R = -1) constant amplitude sinusoidal waveforms for cyclic strain amplitude between 4000 and 12000 microstrain.

Slower cooling rates associated with the oscillation build strategy result in large single variant α colonies with strong crystallographic texture along primary columnar β grain boundaries. Figure 1 (a) shows texture analysis by EBSD showing α phase with continuous $\alpha_{GB}$ colonies (the thick 'pink' region), indicating a strong crystallographic texture with similar orientation either side of the grain boundary. Figure 1 (b) shows micro-XCT with no porosity in the gauge length of a fatigue test sample. This is supported by SEM fractography which found no defects in the fracture faces of any of the broken fatigue test samples.

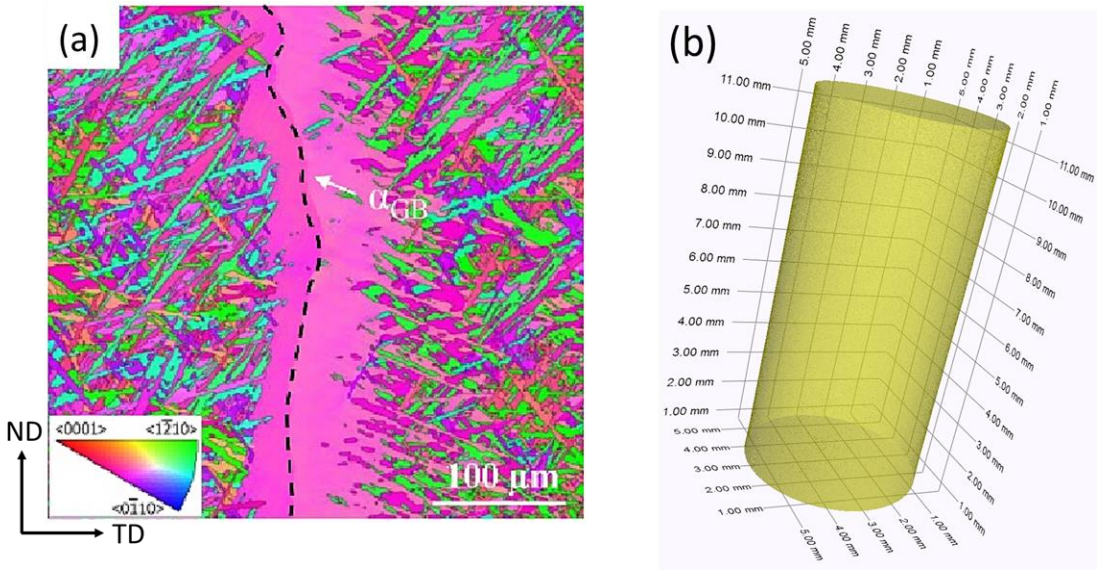


Figure 1 - (a) EBSD texture analysis along a primary β grain, showing α phase with continuous grain boundary α colonies, and (b) Micro XCT analysis showing no porosity in the gauge length of a fatigue sample.

Figure 2 (a) shows the progression of maximum cyclic stress versus normalised load cycles for the horizontal orientation fatigue test samples. In this horizontal orientation the loading axis is parallel to the deposited layers, so is loaded across columnar β grains and $\alpha_{GB}$. In general, cyclic softening is apparent in both this horizontal and vertical (not shown) orientation under different strain amplitudes ($\varepsilon_a$) except when elastic deformation is dominant, $\varepsilon_a \leq 0.6\%$ strain. At higher cyclic strain amplitudes, where $\varepsilon_a > 0.6\%$ strain, three distinct stages are observed (i) initial rapid cyclic softening, (ii) quasi-stable cyclic softening and (iii) rapid progression to failure.

Figure 2 (b) shows that the cyclic softening rate for both horizontal and vertical orientations is similar at lower strain amplitudes, $\varepsilon_a \leq 0.6\%$ strain where elasticity dominates. Above this the cyclic softening rate increases dramatically in both orientations and stabilises with a plateau response. In this region the cyclic softening rate for vertical orientation is approximately 2x higher than the horizontal at the same cyclic strain amplitude.

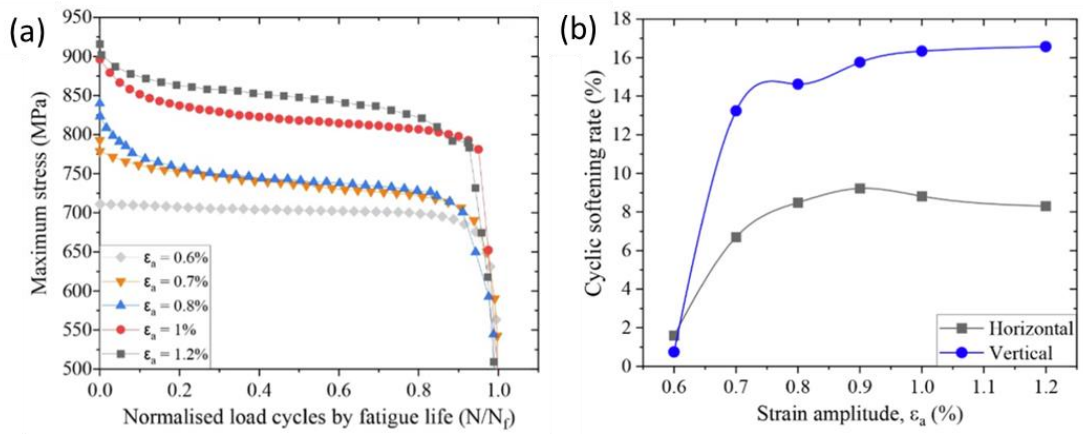


Figure 2 (a) Cyclic maximum stress vs normalised load cycles for horizontal samples, and (b) Cyclic softening rate under different strain amplitudes.

Between the two sample orientations, microstructure heterogeneity leads to tensile property anisotropy:

- Tensile and yield strengths are 5% higher for samples extracted in parallel with the deposition layers (horizontal orientation in the wall), normal to the material build direction.
- Elongation is 50% higher for samples extracted perpendicular to the deposition layers (vertical orientation), in the material build direction.

Cyclic stress softening is observed in both sample orientations when the applied strain amplitude exceeds 0.6% strain. Because of higher ductility, the cyclic softening rate in vertical samples is approximately two times higher when strain amplitude is higher than 0.7% strain.

Fatigue life performance is anisotropic in the low cycle fatigue regime, where the vertical orientation samples have average life about 2.5 times longer than that of the horizontal samples due to higher ductility in the former. In the high cycle fatigue regime fatigue life performance is almost isotropic.

This work is reported in more detail in International Journal of Fatigue, Volume 171, June 2023, “Strain controlled fatigue behaviour of a wire + arc additive manufactured Ti-6Al-4V” and is available from:
https://www.sciencedirect.com/science/article/pii/S0142112323000804

# 6 Corrosion and Fracture Mechanics Modelling Technology

## 6.1 Incorporating Corrosion Related Damage Effects in Mechanical Loading Assessment Improves Aircraft Service Life Prediction

*S. Mellings - BEASY*

Engineering assessments of aircraft have found that structural cracks frequently initiate at dissimilar material interfaces, where galvanic coupling drives localized corrosion. This is typically the consequence of service life predictions being performed using pristine (i.e., 'uncorroded') metal structures, without consideration of the intended service environment or the interplay of corrosion and mechanical stress. This leads to costly structural repairs and decreased aircraft availability.
BEASY is undertaking a collaborative research project to develop and deliver engineering tools that incorporates the interaction of mechanical, environmental, and galvanic stresses when predicting service life of aircraft structures and components. The engineering tool will also guide design and maintenance by overlaying structural load, fatigue susceptibility, environmental conditions, failure points, and predicted galvanically assisted corrosion damage for rapid risk assessment and visualization.
The work has included instrumented corrosion and mechanical test articles - as well as continuous measurements of environmental spectra and mechanical loads - to quantify the initiation and propagation of failure modes. Key developments:

- Development of technology to process data from environmental sensors to provide the Environmental Load spectra data for simulation of Atmospheric corrosion of structures using Galvanic Corrosion Simulation models.

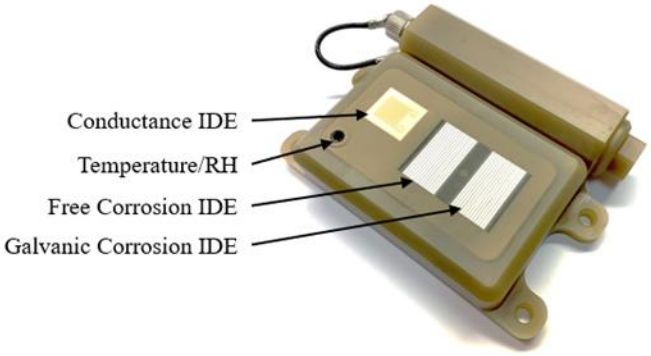


Figure 1 - Environment and corrosivity monitoring device. Luna Labs

- Enhancement and validation of Galvanic Simulation models suitable for the simulation of galvanic corrosion of structures under atmospheric and bulk electrolyte conditions. The models are suitable for the prediction of the location of corrosion on the structure and its severity.

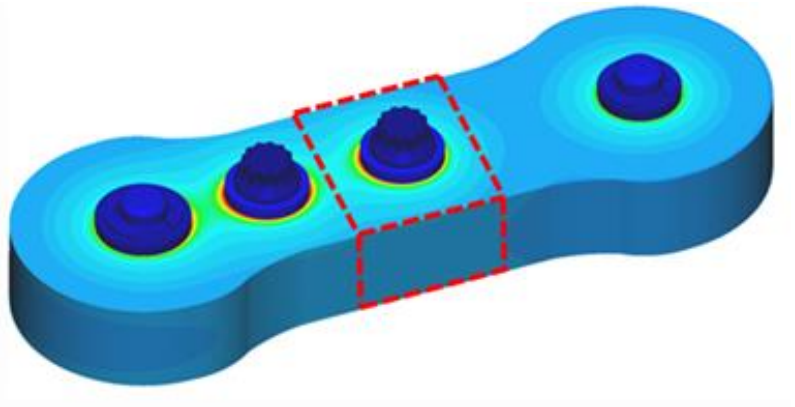

Figure 2 - Predicted galvanic corrosion on test article with fasteners under atmospheric corrosion conditions

- Engineering assessments have found that environmentally assisted cracking occurs more frequently in service than ‘unassisted’ metal fatigue, with a split between stress corrosion cracking and fatigue. BEASY crack growth software is being used to predict the environmental impact of stress corrosion cracking and corrosion fatigue on structures.

Tool development, verification testing, and demonstration studies are being performed using simulated test cycles relevant to sea-based environments, outdoor exposures, and on-aircraft measurements. Initial demonstration of the tools involves case studies for representative part geometries, flight profiles, mechanical load spectra, and environmental load spectra.
This work brings new innovation in the coupling of galvanic modelling technology with dynamic environmental sensor measurement to improve understanding of the critical electrolyte properties that impact the atmospheric corrosion process. As this technology continues to mature it will provide airframe management teams with valuable information to use when deploying assets or planning for maintenance. Understanding and being able to quantify the corrosion performance of critical assets in different environments will improve fleet management practices. Additionally design engineers will gain insight into design durability and be able to evaluate dissimilar metal compatibility in different environments using modelling tools that leverage real-time environmental measurements to guide selection of input parameters.

(The partners in this collaborative research are BEASY, Boeing & Luna Labs and is supported by the ONR Sea Based Aviation Structures & Materials Program, ONR Technical Point of Contact: William Nickerson, Anisur Rahman.)

### 6.2 BEASY Domain Decomposition Solver Dramatically Reduces Crack Growth Solution Times

The Domain Decomposition Method (DDM) solver is a new approach to the creation and the solution of the systems of equations created during a BEASY simulation. In a normal BEASY solve, the BEASY software systems of equations are created for each zone in a model and assembled into a single system of equations which are then solved. These assembled equations require very large amounts of memory and disk storage which limits the size of the model which can be solved. Processing all the equations together also increases the computational resources resulting in long computational times.
The DDM approach enables the computational tasks to be divided into several smaller problems which reduces the memory and disk storage requirements. The DDM solver is designed to work with multi zoned BEASY models, using the Schur Complement to create the interface equations.
Another major benefit of the DDM approach is that a significant percentage of the computations required when solving the model can be performed independently for each of the zones. This means that the solution can be distributed over several computational nodes to reduce the elapsed time required for the simulation. This DDM approach also reduces the size of the system of equations required for the whole model therefore reducing the computer memory requirements.
A successful research project has been undertaken in collaboration with Bournemouth University, to develop the features of this new BEM based solver. This project focused on solving large-scale BEASY models as well as reducing the overall solution time using stand-alone BEASY models with and without cracks.
Further work has since continued implementing this solver into standard BEASY packages. The initial implementation of this new DDM solver, enabled for a single shared memory system, makes partial use of the features available in the DDM solver, with more features planned over the coming software releases.
Based on the test cases run, the shared memory workstation, the simulation elapsed time is proportional to the sum of the squares of the number of degrees of freedom (DOF) in each of the zones in the model. This trend is significant as it suggests the ability to solve much larger models.
This has been proved in a crack growth simulation that uses large, uncracked BEASY model. In this model the solution time for a single step in the crack growth simulation reduced from over 10 hours down to just an hour.

## 6.3 BEASY SIF Solutions Available in AFGROW Using New COM API Interface

Another recent development with the BEASY fracture code is the expansion to providing details from the computed stress intensity factor (SIF) results in a COM form. This allows for developments where customers can access the detailed SIF results from a BEASY crack growth and use them in their own in-house tools.
This has been developed and tested while generating a tie in with the AFGROW package where the SIF results can be used to compute the fatigue life. This package allows for planar views of the crack fronts to be shown within the AFGROW interface.

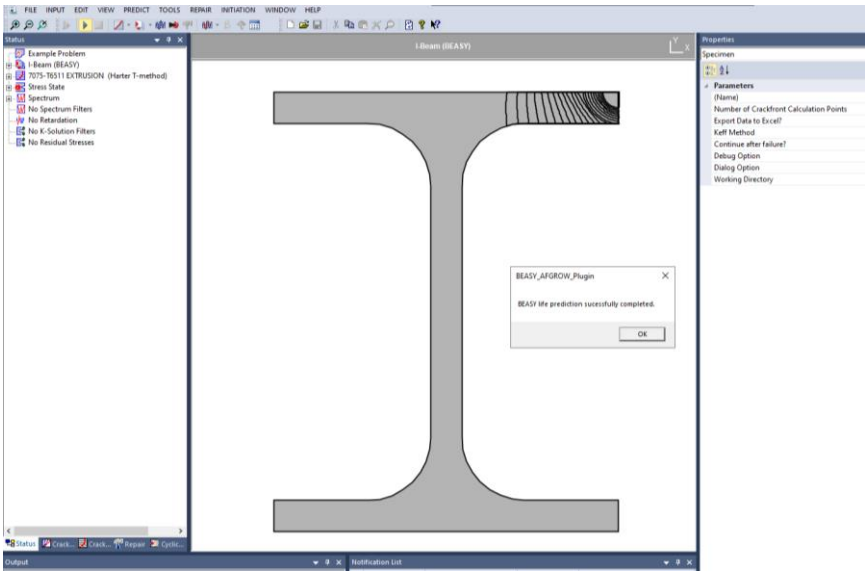


Figure 1 - Plot when the critical SIF is reached.

## 6.4 Crack Merging Simulations Available to Support Multi-Site Damage Applications

At ICAF 2021 we reported on new capabilities when running with multiple cracked models. In cases where cracks are co-planar these can be allowed to merge automatically. In this simulation a number of initial cracks have developed at a hole where a connector is attached. In this specific case no residual stresses have been considered. Initially five cracks were started as shown in Figure 1. These grow automatically under the applied load; the three central cracks first coalesce, as shown in Figure 2, before the fourth joins, as shown in Figure 3. This simulation was terminated just before the final crack merged (Figure 4).

Figure 1 - Initial step with 5 cracks started.

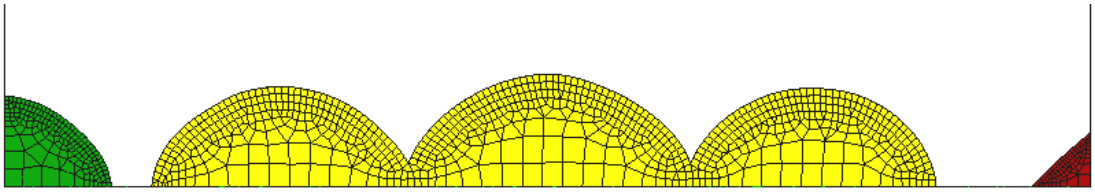

Figure 2 - Three cracks automatically merged during the growth.

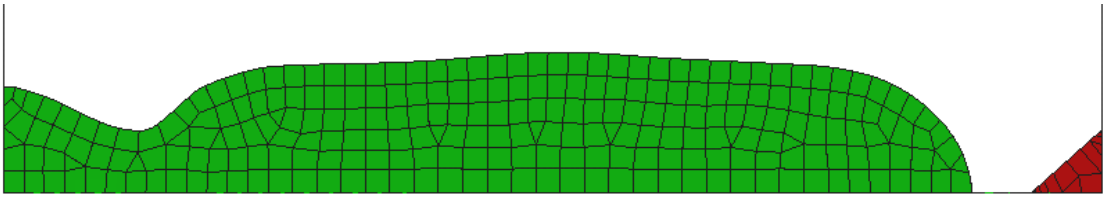

Figure 3 - Fourth crack automatically merging.

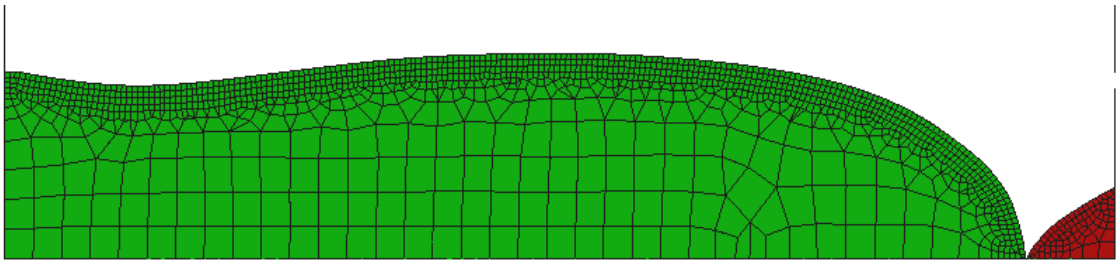

Figure 4 - Fifth crack about to join.

## 6.5 Automatic Crack Growth Using Equation Based Residual Stress

Another development for the crack growth area has been to add equation based residual stress loading. Traditionally a BEASY crack growth model has been able to incorporate residual stress loading; these could be from surface treatments like laser shot peening or from manufacturing processes such as welding. This tool has now been extended to allow piecewise-linear representations of stress fields, where the stress field is defined in terms of a parameter such as the distance from an external surface. This expands the range of use, allowing the effect of residual stresses to be considered for users that don't have access to detailed residual stress fields. This could also be used to investigate "what if" scenarios, investigating the change of the residual stress distribution on the resulting crack profile and fatigue life.

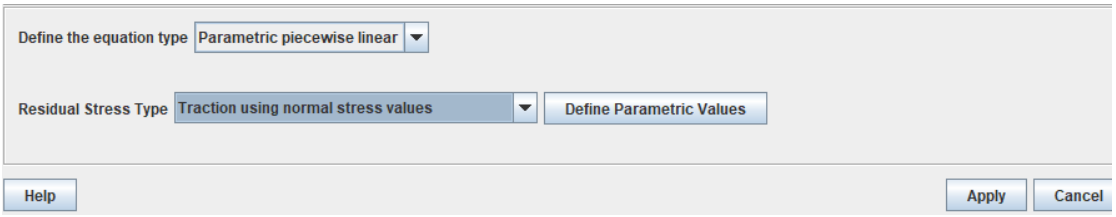


Figure 1 - Traction using normal stress values.

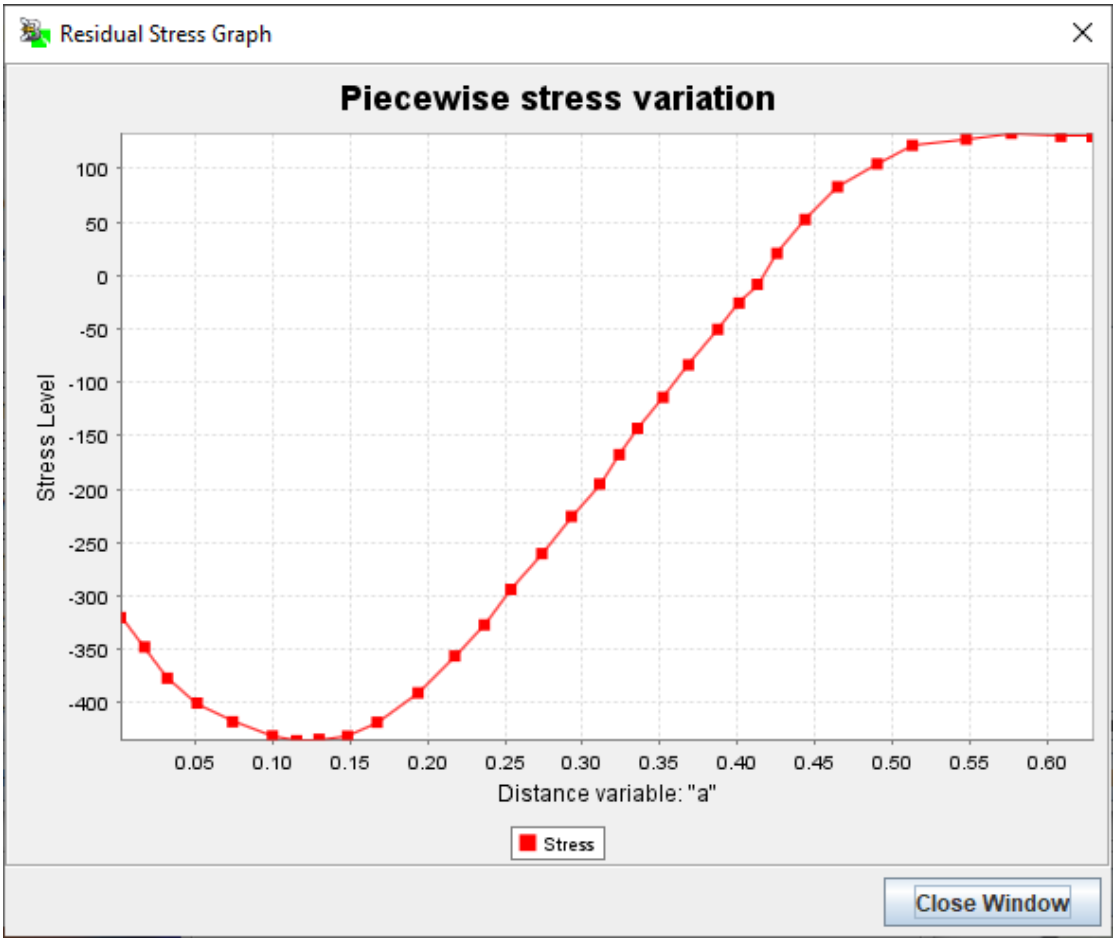


Figure 2 - Graphical view of the stress variation.

## 6.6 Improved Fatigue Modelling Using Time Dependent Flight Blocks

There have been significant developments of "flight" block type loading, where a pre-defined loading sequence is not known but is computed by studying load transitions. In this type of study, the loading sequence is applied, and the resulting fatigue loading cycles are obtained at all points along the crack front.
This technology was developed for investigating the crack growth in landing gear, where different flight schedules are applied but has also been used in the offshore wind turbine area. Further developments have allowed for the results to be presented in terms of the operational time and damage resulting from each of the flight blocks to be reported.

## 6.7 Phase Field Modelling of Stress Corrosion Cracking in Superalloys at High Temperature

*M. Elsherkisi[1], F. Duarte Martinez[1], S. Gray[1], G. M. Castelluccio[1]*

*[1] School of Aerospace, Transport and Manufacturing, Cranfield University, Bedfordshire, UK*

The reliability of turbine engines strongly depends on the environment through which aircraft fly. Humidity, contaminants, operating stresses, and temperatures determine the likelihood of cracking. Simultaneous crack initiation at multiple locations leads to crack interaction, either in the form of shielding or coalescence, which has the potential for arresting damage or accelerating catastrophic failures.

Phase Field models were used to evaluate crack propagation and crack interaction in CMSX-4 C-Ring tests. The model assumes that contaminants diffuse and reduce the material's critical energy release rate, which enables crack propagation. The model, which is calibrated to enable cracking above threshold stress, predicts the crack spacing needed to see crack shielding or coalescence. It was found that parallel cracks with spacing below 200 µm saw a crack shielding effect, whereby the local crack tip stresses were drastically reduced, and such stopped any further propagation. Above this critical threshold and cracks would see no interactions. However, between 1 and 10 µm, a stress intensification was seen such that crack coalescence, or crack tip merging, was possible. These simulations led to novel experiments being designed to prove shielding effects, the first being the ‘Zebra C-Ring’ test, which was designed with one goal in mind: minimise crack interaction and therefore encourage crack growth. Sections of the surface were taped off before being exposed to the salt spray and placed in the SO2-

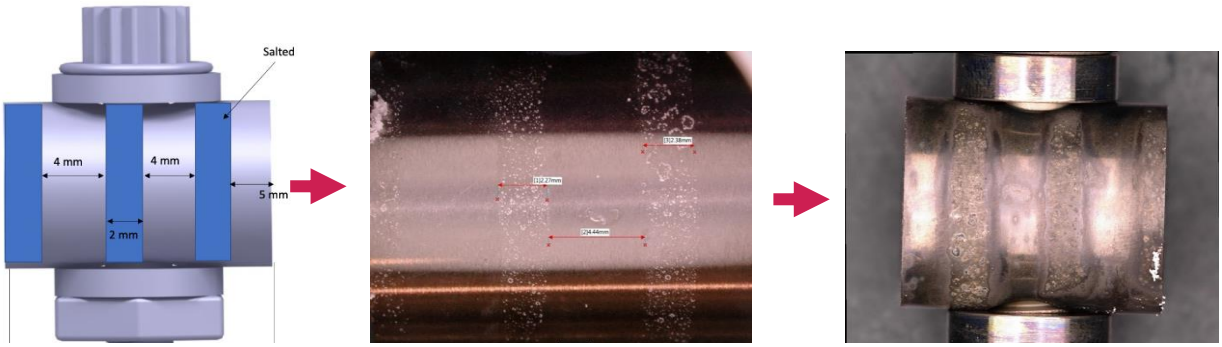


Figure 1 - A schematic representing the 'zebra' striped experiment that was designed based on modelling knowhow.

containing furnace. This test saw crack lengths drastically increase from 300 µm (in the previous tests) to over an mm and were consistently spaced by over 200 µm (figure 1).

Next, the design was redefined to minimise the chances of multiple crack initiation sites even further, and this led to the '3 Dot' test. A micro-pipette was used to place three well-spaced salt droplets (with varying concentrations) on the C-Ring's surface before the same furnace, under the same environmental conditions. Crack interactions were now minimised so much that cracks reached lengths over 2.5 mm, and hence proved that crack interaction has a significant on the extent of cracking under stress corrosion conditions. The results are highlighted in the below figure 2.

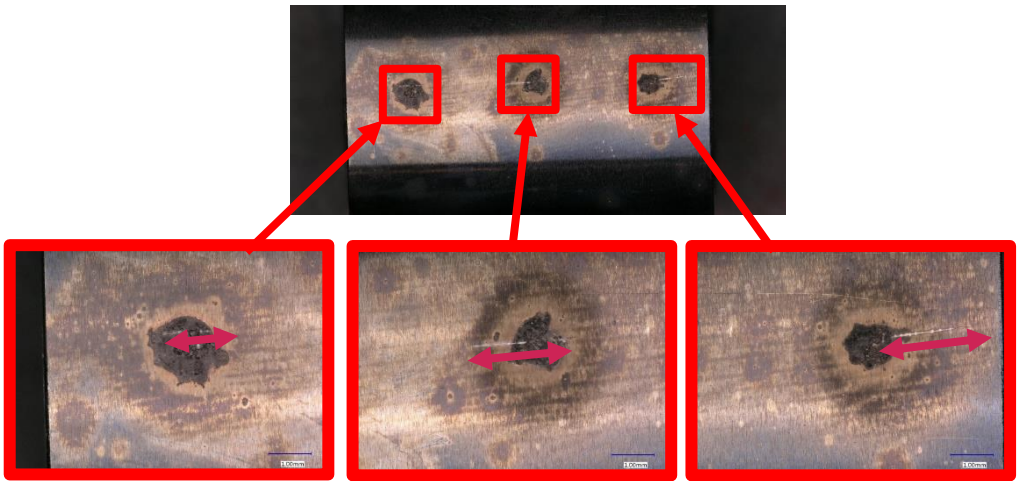

Figure 2 - Optical images to show the extent of cracking for each site of varying salt concentration with a) being an overview and b, c, and d representing 1x, 2x, and 4x salt flux respectively.

## 6.8 Integration of X-Ray Microscopy and Finite Elements into a Digital Twin

*M. Elsherkisi[1], S. Dhimal[1], M. Kothari[2], F. Duarte Martinez[1], S. Gray[1], G. M. Castelluccio[1]*

*[1] School of Aerospace, Transport and Manufacturing, Cranfield University, Bedfordshire, UK*

*[2]Carl Zeiss Microscopy*

X-Ray microscopy (XRM) has revolutionised materials characterization with impressive details and resolution. However, materials responses depend on a myriad of attributes that cannot be entirely characterised by a single device. Thus, computational modelling can complement experimental efforts by providing estimations of attributes (e.g., stress) concurrent with the material characterization.

This work focused on the integration of XRM with finite element models (FEM) to enable the mapping of real-life cracks that are translated to realistic model meshes. We will demonstrate that the approach has been instrumental in univocally discovering the damage mechanism involved in stress corrosion cracking. An autonomous integration

approach between XRM and FEM was developed which can be implemented concurrently with the material characterisation. The seamless XRM-FEM exchange has the potential to control experiments based on magnitudes that are not measured but modelled (figure 1).

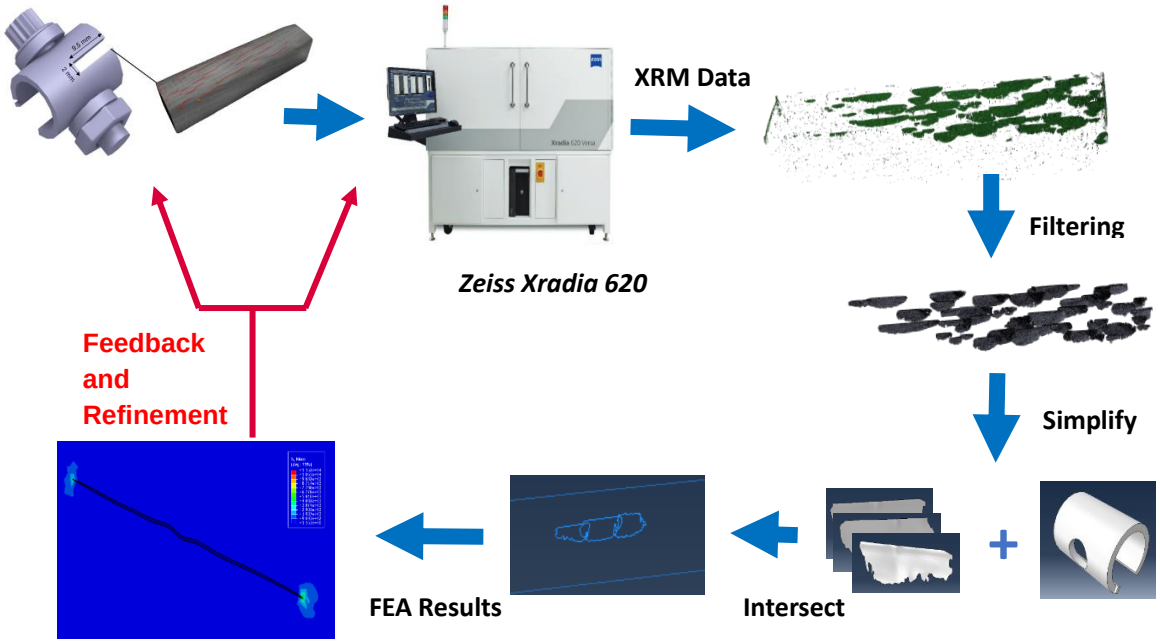


Figure 1 - Flow chart summarising the key stages and programmes used to create a 3D crack approximation.

This workflow was used to digitalise cracks from a C-Ring which was exposed to stress corrosion conditions. These C-Rings were coated with a NaCl salt solution and displaced to produce a peak stress distribution and exposed to a 550C in an air + $SO_2$-containing environment. The now cracked C-Ring was scanned using an XRM and the data entered the workflow, and 25 of the total 60 cracks were digitalised to run FEA. A plasticity-based model was run to produce a stress (Von Mises) distribution map surrounding these 25 cracks, and the results are highlighted below. There were clear regions of both crack tip stress reduction and intensification, caused by crack shielding and coalescence respectively. It is postulated that should the sample be placed back in the furnace with this given crack formation, the areas of intensification (highly red contoured regions) would potentially see crack tip merging (figure 2).

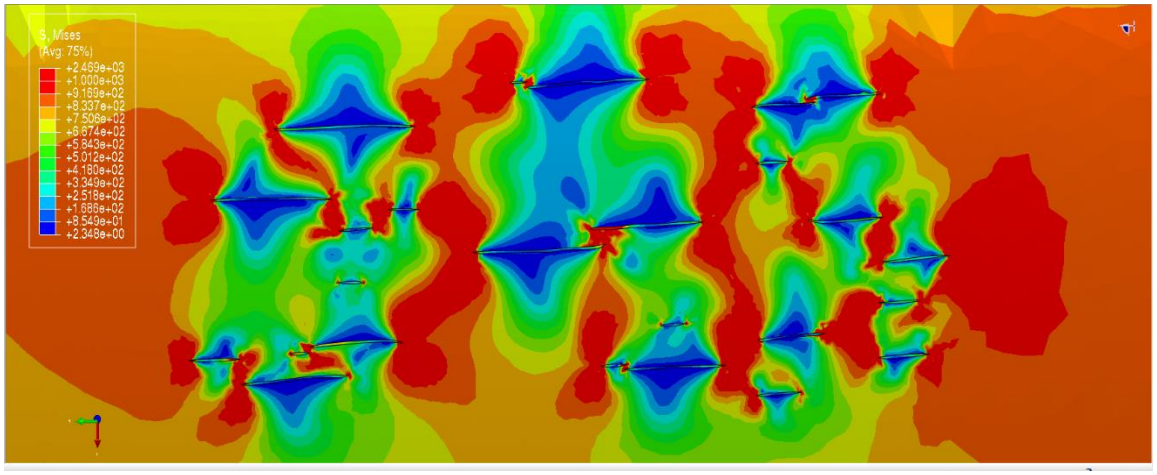


Figure 2 - A Von Mises stress plot that represents the stress distribution for the given crack formation.

# 7 Structural Health and Usage Monitoring

## 7.1 A Low-Cost Structural Health Monitoring Device Exploiting Full-Field Imaging Techniques for Fatigue Damage Detection in Aerospace Structures

*Ceri A. Middleton* and Eann A. Patterson*
*School of Engineering, University of Liverpool, The Quadrangle, Brownlow Hill, Liverpool L69 3GH, UK*
**ceri.middleton@liverpool.ac.uk*

### 7.1.1 Introduction

The early detection of damage in engineering structures during testing and in-service use is necessary for repair, replacement and/or redesign to be carried out. A range of NDE (non-destructive evaluation) techniques exist which can be used for structural health monitoring (SHM) and fatigue damage detection. These techniques include point-source and full-field techniques, where full-field techniques collect information from a larger region of interest than point-source techniques. For example, thermoelastic stress analysis (TSA) results in a map of surface stresses [1], whereas a map of strain can be calculated using digital image correlation (DIC) [2]. Areas of high strain or stress in these maps indicate locations where damage has occurred or may occur in the future, so monitoring changes in these maps over time will show how fatigue damage evolves.

The interpretation of full-field datasets, often presented as images, can be labour intensive, and when considering long tests or in-service use, a large number of datasets must be analysed. One approach towards a more automated interpretation is the use of orthogonal decomposition. This technique takes a two-dimensional dataset and describes it using a one-dimensional feature vector that is orders of magnitude smaller than the original dataset [3], [4].

Feature vectors therefore require less storage space than the original data, which is an important consideration if arrays of full-field sensors are to be deployed over months or years for long timescale testing or in-service use. It is also possible to use the feature vectors for quantitative comparisons between those datasets. By calculating the difference between the feature vectors representing two images, with the first (reference) image at a low or zero damage state, a measurement of how much those images differ can be found, thereby indicating changes due to damage appearance or growth.

Work carried out in the Horizon 2020, Clean Sky 2 project INSTRUCTIVE (INfrared STRUctural monitoring of Cracks using Thermoelastic analysis In production enVironmEnts) [5] showed the use of orthogonal decomposition of TSA data-fields to generate a quantitative measurement of crack growth during cyclic and flight-cycle fatigue loading. This work was compared to previously published crack length measurement methods, indicating that the decomposition technique gives comparable results to established approaches (Figure 1).

Data were initially collected with a traditional, high resolution photovoltaic detector, but the use of packaged and OEM (original equipment manufacturer) microbolometers was

also explored, demonstrating that data from smaller, cheaper detectors could also be used with this approach, to produce a quantitative measure of damage propagation over time.

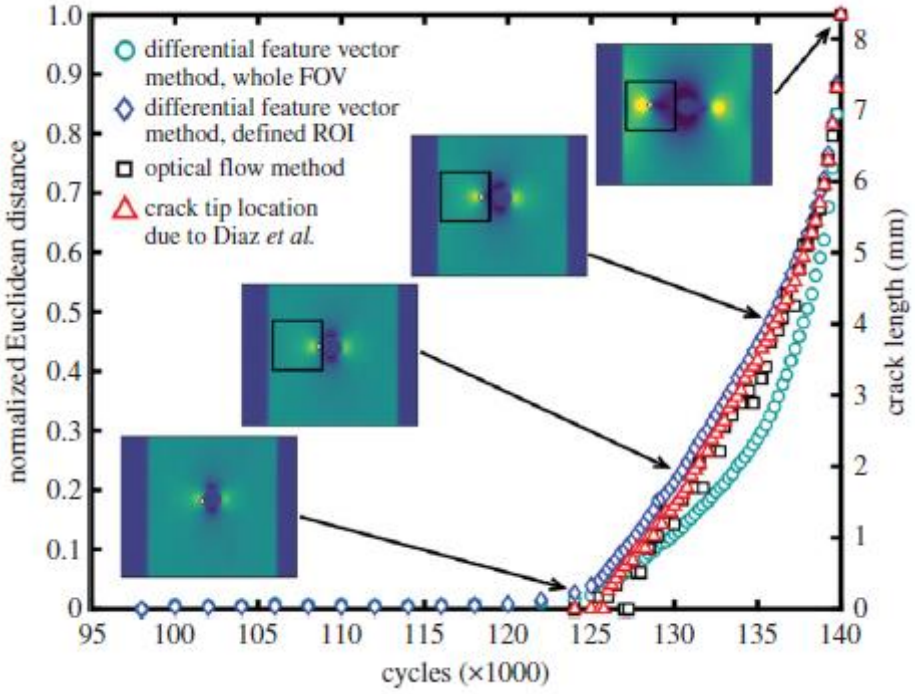


Figure 1 - Feature vector difference (normalised Euclidean distance) against load cycles during fatigue crack growth monitored by TSA, insets show uncalibrated TSA maps at given times. Comparison with previous analysis (optical flow, Middleton *et. al.* [6]) and crack length measurement method from the literature (Diaz *et. al.* [7]). Figure from [5].

Technological developments in board computers and sensors have introduced the possibility that these techniques can be applied in industrial environments which were previously not possible due to spatial or budgetary constraints. The use of these centimetre-size sensors was explored further in the Horizon 2020, Clean Sky 2 project DIMES (Development of Integrated MEasurement Systems).

### 7.1.2 Low-cost SHM system

COTS (commercial-off-the-shelf) components were integrated to construct a sensor system which combines visible and infrared imaging with input from a resistance strain gauge (RSG). Sensor units, comprising a sensor module and a board computer module (Figure 34) can be deployed at regions of interest and connected to a control computer and network attached storage (NAS) server, which can be installed at a distance from the test object. Power and data transfer is achieved through an ethernet cable, and input is taken from a RSG installed locally to the field of interest. Several sensor units can be linked to one control computer, and a bespoke graphical user interface allows a user to both control data collection and access and visualise stored data.

Processing of infrared images makes use of the thermoelastic effect, but is uncalibrated, so is referred to here as CATE (Condition Assessment by Thermal Emissions), to distinguish from traditional TSA processing approaches. Raw data in the form of visible and infrared images are collected, and combined with RSG values and processed locally on the board computer (Raspberry Pi) to generate DIC and CATE outputs respectively. These datasets are processed further using orthogonal decomposition, resulting in a feature vector difference which can be monitored for indications of damage initiation and propagation.

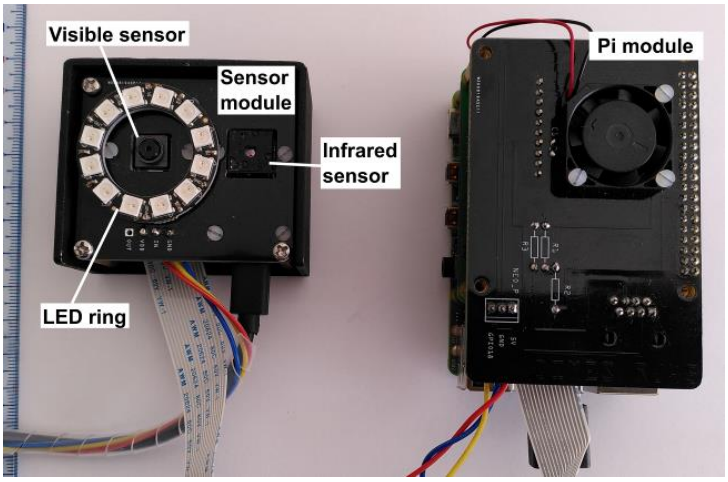


Figure 2 - Sensor unit assembled from COTS components: sensor module (left) contains visible and infrared imaging sensors; board computer (Raspberry Pi) module (right). Scale in mm, from [8].

### 7.1.3 Laboratory testing

This system has been tested in the laboratory on coupon specimens, with a particular focus on data processing for extraction of damage information using the thermoelastic effect. Amjad *et. al.* [9] showed that results from the OEM microbolometer are similar to those of the higher resolution photovoltaic detector for damage detection during cyclic loading, although crack detection occurs earlier with the higher resolution sensor.

As the cheaper infrared sensors have lower spatial, temporal, and thermal resolutions than sensors used for traditional thermographic techniques, delayed crack detection is not surprising. However, a slight delay in detection (on the order of millimetres) is likely to be offset by advantages in size, cost and replaceability of the OEM sensors (£100s) when compared to photovoltaic detectors (£10,000s).

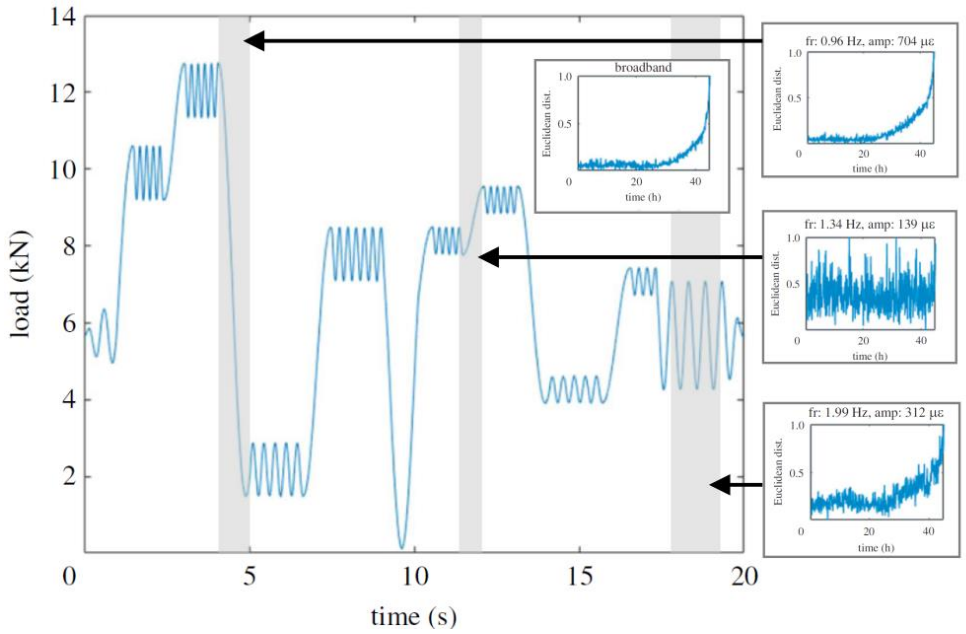


Figure 3 - Representative flight-cycle load. Insets show feature vector difference for given sections of the cycle. Adapted from [9].

The data processing algorithms have also been applied to data collected during flight-cycle loading, which is more representative of real-life conditions experienced by an aeroplane in flight (Figure 3). Amjad *et. al.* [9] found that analysis of CATE data collected during crack growth caused by repeated loading of the flight cycle also resulted in a feature vector difference indicative of damage growth. This feature vector difference could be extracted from a broadband analysis of all data, but was also found when certain sections of the flight cycle were analysed separately (Figure 3).

### 7.1.4 Industrial deployment

This prototype SHM system was deployed on full-scale airframe tests, including a fuselage pressurisation test at Airbus in Toulouse. A sensor unit was installed at a known crack site (Figure 4), and data was collected over a period of several weeks. DIC strain data were successfully output from the sensor system, indicating the location of the crack. Growth of the crack was observed in the strain maps, and a subsequent increase in the feature vector difference was also seen (Figure 5) [8].

Figure 4 - Installation of a sensor unit in the full-scale fuselage test, from [8].

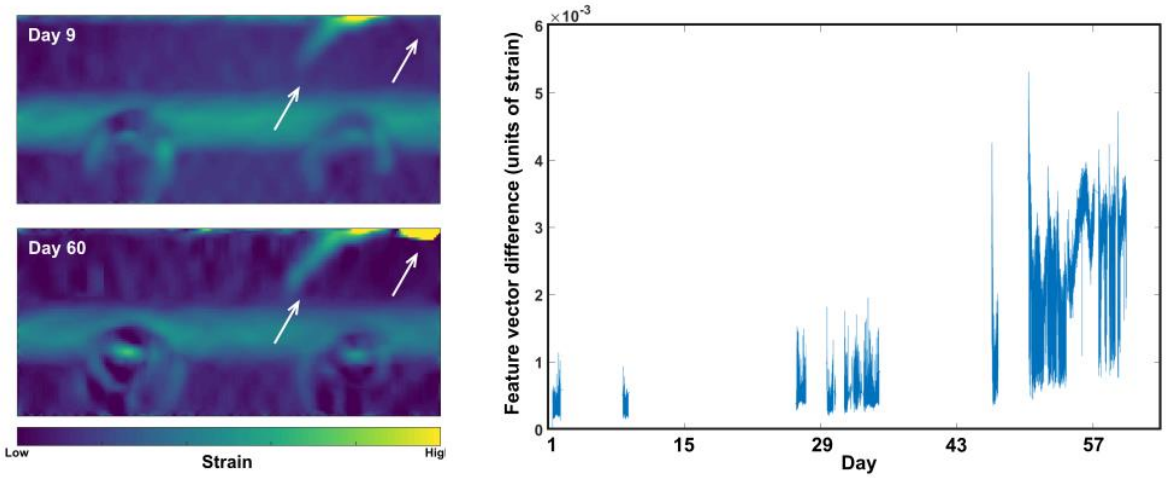


Figure 5 - DIC strain maps at two dates during data collection, arrows indicate initial crack location and growth, and development of a secondary crack (left). Feature vector difference over time calculated by decomposition of strain maps (right). Adapted from [8].

### 7.1.5 Summary

A low-cost SHM system has been developed, making use of COTS technologies and advanced data processing techniques. Centimetre-sized visible and infrared imaging sensors have been combined with a board computer to assemble a low footprint unit which is deployed at the region of interest. Data processing occurs in near real-time, on board the unit, outputting DIC and CATE data-maps. These full-field outputs are further processed using orthogonal decomposition to give a quantitative measurement of the changes observed, representing the growth in fatigue damage in the field of view.

This system has been deployed on full-scale airframe tests, successfully collecting and processing data in near real-time. In a full-scale fuselage test, the location of damage and growth of that damage was indicated, demonstrating that this system represents a step towards in-service condition monitoring using these full-field techniques.

## Acknowledgements

This work received funding from the Clean Sky 2 Joint Undertaking under the European Union's Horizon 2020 research and innovation programme under grant agreement Nos. 686777 and 820951. The opinions expressed here reflect only the authors' view and the Clean Sky 2 Joint Undertaking is not responsible for any use that may be made of the information it contains.

## References

[1] R. J. Greene, E. A. Patterson, and R. E. Rowlands, "Thermoelastic stress analysis," in *Springer Handbook of Experimental Solid Mechanics*, W. N. Sharpe, Ed. Springer, 2008, pp. 743–767.

[2] M. Sutton, J.-J. Orteu, and H. Schreier, *Image correlation for shape, motion and deformation measurements*. Springer, New York, 2009.

[3] C. M. Sebastian, E. López-Alba, and E. A. Patterson, "A comparison methodology for measured and predicted displacement fields in modal analysis," *J. Sound Vib.*, vol. 400, pp. 354–368, 2017.

[4] W. J. R. Christian, K. Dvurecenska, K. Amjad, J. Pierce, C. Przybyla, and E. A. Patterson, "Real-time quantification of damage in structural materials during mechanical testing," *R. Soc. Open Sci.*, vol. 7, no. 3, 2020, doi: 10.1098/rsos.191407.

[5] C. A. Middleton, M. Weihrauch, W. J. R. Christian, R. J. Greene, and E. A. Patterson, "Detection and tracking of cracks based on thermoelastic stress analysis," *R. Soc. Open Sci.*, vol. 7, no. 12, 2020, doi: 10.1098/rsos.200823.

[6] C. A. Middleton, A. Gaio, E. A. Patterson, and R. J. Greene, "Towards Automated Tracking of Initiation and Propagation of Cracks in Aluminium Alloy Coupons Using Thermoelastic Stress Analysis," *J. Nondestruct. Eval.*, vol. 123, no. 38:18, 2019, doi: 10.1007/s10921-018-0555-4.

[7] F. A. Díaz, J. R. Yates, and E. A. Patterson, "Some improvements in the analysis of fatigue cracks using thermoelasticity," *Int. J. Fatigue*, vol. 26, no. 4, pp. 365–376, 2004, doi: 10.1016/j.ijfatigue.2003.08.018.

[8] C. A. Middleton *et al.*, "Application of a low-cost structural health monitoring system to full-scale aerospace testing," in *ETTC - 2023 European Test & Telemetry Conference*, 2023.

[9] K. Amjad, P. Lambert, C. A. Middleton, R. J. Greene, and E. A. Patterson, "A thermal emissions-based real-time monitoring system for in situ detection of fatigue cracks," *Proc. R. Soc. A Math. Phys. Eng. Sci.*, vol. 478, no. 2266, 2022, doi: 10.1098/rspa.2021.0796.

## 7.2 Remote Sensing of Aerospace Usage Profiles via Air Traffic Data

*Josh Hoole, Julian Booker, Jonathan Cooper, Tom Richardson*
*Faculty of Engineering, University of Bristol, United Kingdom, email: josh.hoole@bristol.ac.uk*

### 7.2.1 Background

During the fatigue design of aerospace structures and components, the definition of accurate usage spectra is a challenging task due to the high levels of variability present within aerospace operations [1,2]. Such variability can lead to significant assumptions being necessary when considering fleet-wide usage profiles or the adoption of standardised fatigue spectra [3,4].
'Real-time' tracking of aerospace vehicles has recently become a reality through the crowd-sourcing of Automatic Dependent Surveillance-Broadcast (ADS-B) air traffic data [5]. ADS-B data provides a 3D trajectory of aircraft flights, and providing ground-based receiver coverage is available, can be applied remotely across entire global fleets [3]. Regarding the work in the wider field by other institutions, the rapid growth in crowd-sourced air traffic data has the potential to provide the required insight for adopting new technologies and system architectures. Examples of such investigations are presented in prior studies concerning regional aircraft electrification [6] and the exploitation of ADS-B data for the usage monitoring of helicopter gearboxes [7].
The University of Bristol has previously explored the use of ADS-B data to enhance the characterisation of landing gear ground manoeuvre spectra [3] and work performed since the previous ICAF UK review has continued to investigate the utility of ADS-B for defining manoeuvre occurrences in-flight to support the challenge and verification of existing standardised spectra.

### 7.2.2 Case Study: Helicopter Flight Manoeuvre Statistics

The Helix and Felix spectra are long-established load spectra for Helicopter rotor blades and consist of blocks of different rotorcraft manoeuvres and their occurrence assembled into a standardised fatigue spectra [4]. A case study performed by the University of Bristol [3] considered the ADS-B trajectories from a fleet of nine twin-seat training helicopters. Within this case study, conditional algorithms were developed to identify the manoeuvres performed within the trajectory (including rotorcraft specific manoeuvres such as autorotation and hover) as shown in Figure 1.

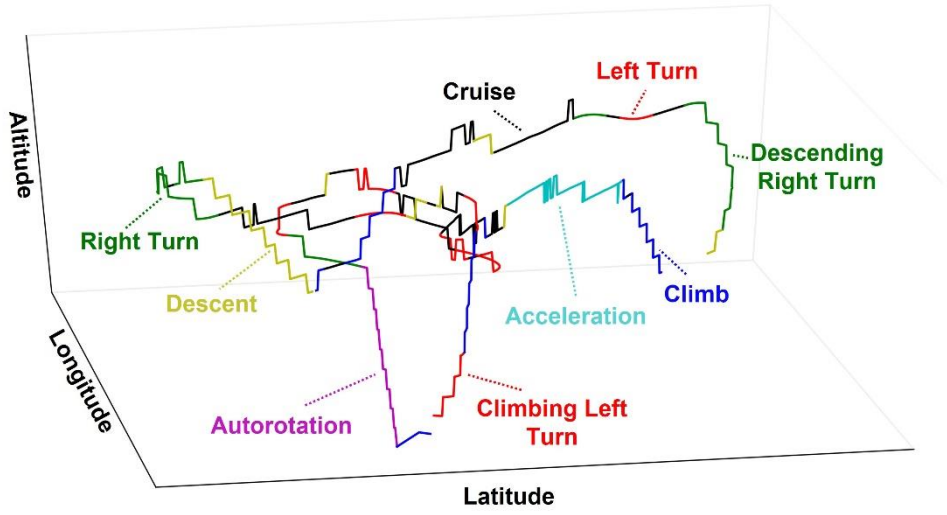


Figure 1 - A training helicopter flight ADS-B trajectory with identified manoeuvres labelled [2] CC BY 4.0.

An annual dataset for each airframe was considered, resulting in the collection of 2,355 flights from the OpenSky Network [5]. When processed through the developed algorithms, the occurrence of specific manoeuvres could be identified and compared to the Helix and Felix spectra. Full results have been reported [2] and below is a summary of key findings:

- The average number of turning manoeuvres per flight was below that assumed within Helix/Felix, but there is significant turning occurrence variability, see Figure 2(a), and a large number of different turn types as shown in Figure 2(b) not currently featured in the spectra.
- The occurrence of hover manoeuvres was highly skewed, with the majority of hover manoeuvres corresponding to pivot turns, as shown in Figure 3(a) and 3(b) respectively.
- Whilst the average occurrence of 2 autorotation manoeuvres per flight is consistent with the Helix and Felix spectra, there is significant variability in the number of autorotation manoeuvres per flight, see Figure 4(a). Previous spectra have omitted the fatigue-critical S-turn/control reversal autorotation manoeuvres and this is supported by the low occurrence of S-turn autorotation manoeuvres shown in Figure 4(b).

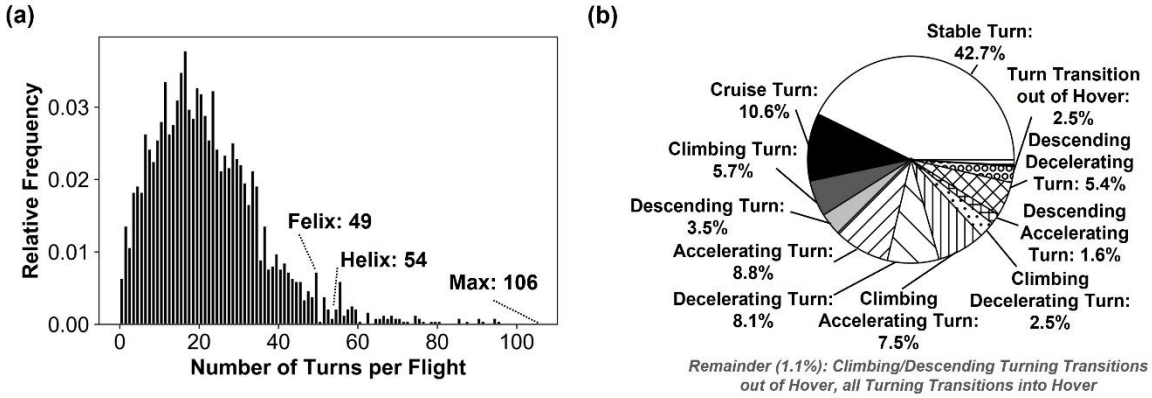


Figure 2 - (a) Variability in turning occurrences per flight. (b) proportional share of turn type [2] CC BY 4.0.

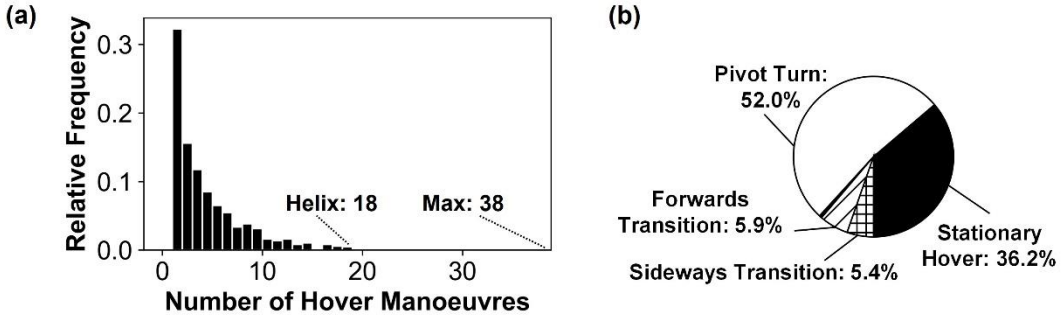


Figure 3 - (a) Occurrence of helicopter hover manoeuvres for flights with hover manoeuvres. (b) proportional share of hover type [2] CC BY 4.0.

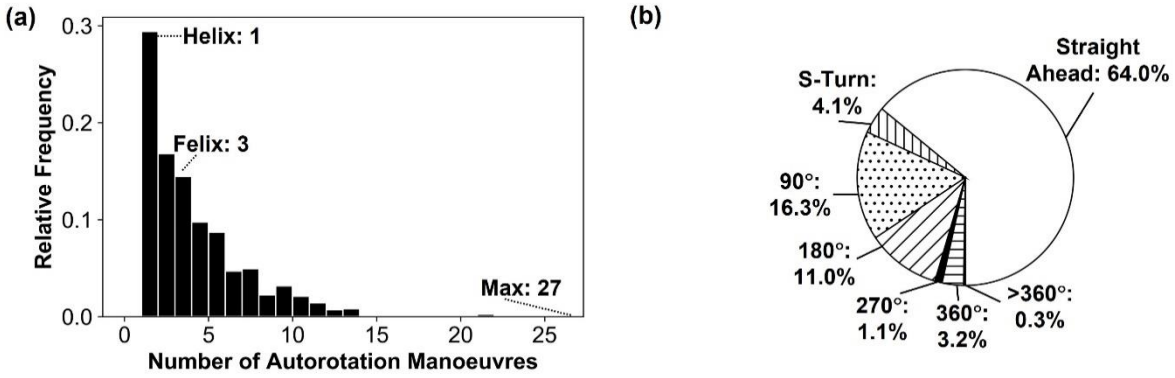


Figure 4 - (a) Variability in autorotation occurrences for flights with autorotation manoeuvres. (b) proportional share of autorotation recovery type [2] CC BY 4.0.

Whilst the exploitation of ADS-B trajectories enabled elements of the pre-existing standardised spectra to be challenged or verified [2], the case study also highlighted the currently limited low altitude ADS-B coverage leading to incomplete flight profiles and challenges related to characterising hover manoeuvres based solely on helicopter ground track rather than heading.

### 7.2.3 Future Outlook

The University of Bristol's focus will continue to explore how air traffic data can be used to support structural integrity assessments of aerospace systems, including those that historically have had limited in-service monitoring such as General Aviation [8]. Within the UK, regulatory changes have facilitated the adoption of lower cost ADS-B transceivers for light aircraft [9] and this has presented a significant opportunity for characterising the usage spectra variability of this sector.
Whilst air traffic data can provide fleet-wide remote monitoring of aerospace vehicle trajectories, it is of course limited in the detail it provides regarding system and structural usage. To explore whether statistical models can be used to infer detailed flight recorder data from ADS-B trajectories, the University of Bristol intends to employ their DG-1000 glider, see Figure 5(a). The comprehensive avionics suite onboard the DG-1000 permits the capture of air data and airframe accelerations which can then be linked to the recorded ADS-B trajectory. Example trajectories are shown in Figure 5(b) and 5(c). Such an investigation could explore the feasibility of remote monitoring and fatigue cycle counting of aerospace structures through air traffic data.

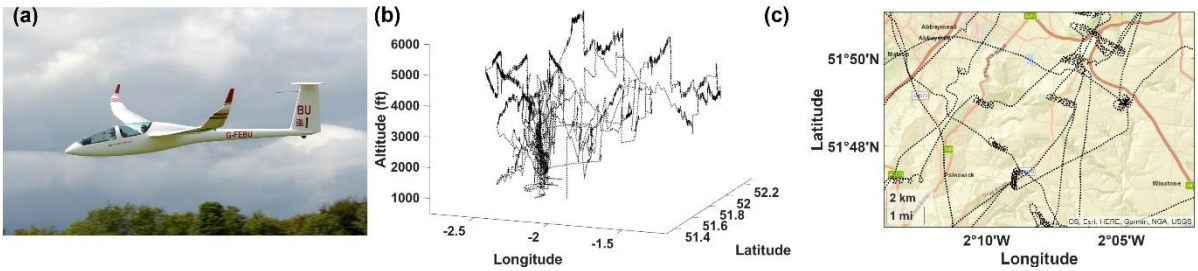


Figure 5 - (a) DG-1000 Glider G-FEBU equipped with ADS-B. (b) ADS-B trajectories for flights of G-FEBU. (c) ADS-B ground tracks of G-FEBU.

## References


[1] Hoole, J., *Probabilistic Fatigue Methodology for Aircraft Landing Gear*, PhD Thesis, University of Bristol, 2020

[2] Hoole, J., Booker, J. D. and Cooper, J. E., "Helicopter Flight Manoeuvre Statistics via ADS-B: An Initial Investigation Using the OpenSky Network", Engineering Proceedings, vol. 13, no. 1, 2021

[3] Hoole, J., Sartor, P., Booker, J. D., Cooper, J. E., Gogouvitis, X. V. and Schmidt, R. K., "Landing Gear Ground Manoeuvre Statistics from Automatic Dependent Surveillance-Broadcast Transponder Data", The Aeronautical Journal, vol. 125, no. 1293, pp. 1942-1976, 2021

[4] Edwards, P. R. and Darts, J., *Standardised Fatigue Loading Sequences for Helicopter Rotors (Helix and Felix), Part 1: Background and Fatigue Evaluation*, Royal Aircraft Establishment, 1984

[5] Schäfer, M., Strohmeier, M., Lenders, V., Martinovic, I. and Wilhlem, M., "Bringing Up OpenSky: A Large-scale ADS-B Sensor Network for Research", Proceedings of the 13th IEEE/ACM International Symposium on Information Processing in Sensor Networks, pp. 83-94, 2014

[6] Jux, B., Foitzik, S. and Doppelbauer, M., "A Standard Mission Profile for Hybrid-Electric Regional Aircraft based on Web Flight Data", Proceedings of the 2018 IEEE International Conference on Power Electronics, Drives and Energy Systems (PEDES), 2018

[7] Hünemohr, D., Litzba, J. and Rahimi, F., "Usage Monitoring of Helicopter Gearboxes with ADS-B Flight Data", Aerospace, vol. 9, no. 647, 2022

[8] Ocampo, J., *et al*., "Development of a Probabilistic Linear Damage Methodology for Small Aircraft", Journal of Aircraft, vol. 48, no. 6, pp. 2090-2106, 2011

[9] *Electric conspicuity devices CAP 1391*, UK Civil Aviation Authority, 2021

# 8 Advanced Repair and Coating Technologies

## 8.1 Assessment of Chromate Free Alternatives as Paint Primers

*J N Patel*
*QinetiQ Cody Technology Park, Ively Road, Farnborough, GU14 0LX, UK*

*This work will be presented during the ICAF 2023 Conference and Symposium.*

Chromate-based primers are widely used on aircraft to protect the aluminium structure from corrosion. Strontium chromate compound has been authorised under REACH legislation but the authorisation is time limited to 7 years, from the sunset date of January 2019.
A search for chromate-free alternatives is known to be conducted by the various aircraft manufacturers. However, this effort is considered to be largely confined to new rather than legacy aircraft. A suitable alternative found may be unique for the aircraft manufacturer and which may not be appropriate for the military fleet that operates aircraft from several different manufacturers.
The current UK National Standard for procuring paint primers, BS 2X 33, specifies a strontium chromate formulated product. In addition, the corrosion test specified in BS 2X 33 is also considered to be affected by REACH legislation. It is also widely considered that the set of standardised current test methods would not adequately predict the performance of the novel chromate-free primers.
A new or revised standard is required for chromate-free primers that is acceptable nationally. There is therefore a requirement to (a) evaluate suitable test methods and (b) to use the developed test protocol for evaluating chromate-free primers for aerospace purposes. For this purpose, a draft test protocol was agreed with stakeholders including aircraft manufacturers', paint manufacturers' and interested members of British Standard Committee responsible for paints for aerospace purposes.
The test programme comprised of tests for assessing colour, gloss, artificial and natural weathering, adhesion, flexibility, fluid resistance and corrosion resistance properties. Some of the corrosion tests were conducted with exposure periods up to 6000 hours and included the chromate containing primer that was used as a control, to compare the results from the chromate-free products. The candidate products were applied onto un-treated 2024-T3 and 7075-T6 aluminium as well as commercially available chromate-free pre-treatments for aluminium alloys.
The laboratory work is nearing completion with a report being prepared. Simultaneously, the test programme and the results obtained are expected to be used for drafting a new national standard for chromate-free primer paint system for aerospace purposes.

## 8.2 Modelling and Optimising Micro-Nozzle Resin Injection Repair of Impacted Composites using CFD

*Ahmed Asiliskender*
*Imperial College London ahmed.asiliskender14@imperial.ac.uk*

The primary aim of this work is to improve the efficiency and reliability of micro-nozzle resin injection repair (RIR) used on impacted composite structures through investigating and developing novel methods in order to quantitatively assess and optimise the resin injection process through modelling and simulation. A procedure we have developed is

to; reconstruct damage geometries using ultrasonic C-scan, simulate resin flow virtually by modelling the damage zone as a porous medium, and iterate through the inlet/outlet configurations in order optimise the fill efficiency.
Due to impracticality and high cost of 3D reconstruction and simulation in the near future, a reduced-order, two-dimensional method is proposed as part of this project which drastically reduces the cost of reconstruction and simulation. Such a method works by assessing the damage on a composite from a top-down 2D perspective using ultrasonic C-scan technique, in individual depth layers (Figure 1). The thickness of damage detected in each layer is estimated and adds to a post-damage thickness map of the composite (Figure 2), and is compared to the composite specimen's thickness before damage in order to create a porosity field, which is used to delineate the damage zone (Figure 3). The obtained porosity field is applied to a constitutive equation in order to create a permeability field (Figure 4), for use directly in the porous flow physics model (Darcy's Law) in a CFD application, thus providing a prediction on the filling of the damage zone. The verification of the physics models used for these simulations are also a contribution of this project in the form of a proposed and analytically solved simulation test case.

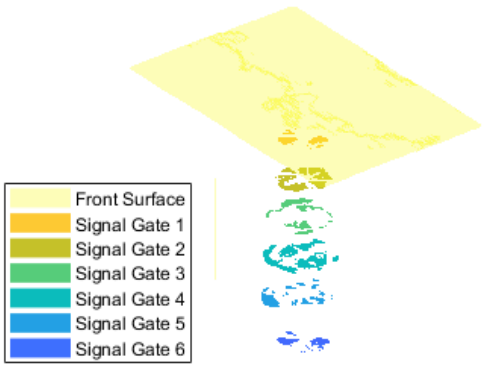


Figure 1 - Damage layer scan.

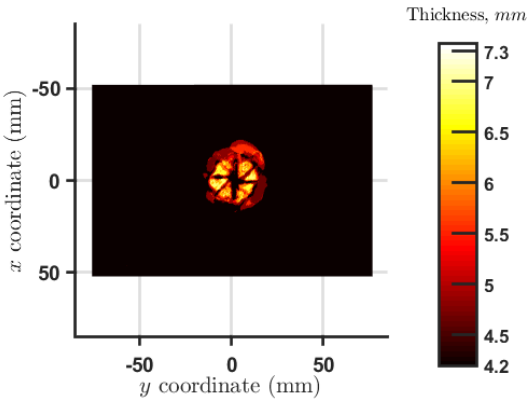


Figure 2 - Post-damage thickness field.

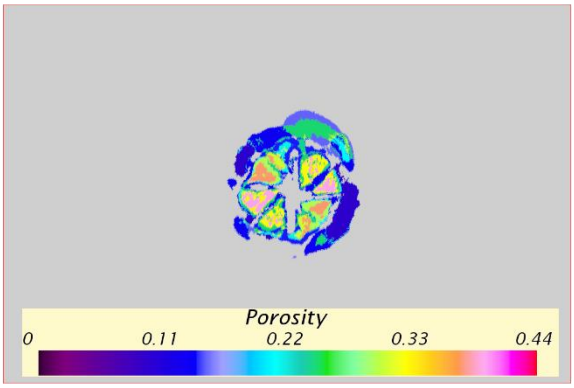


Figure 3 - Filtered porosity map, also shows damage geometry.

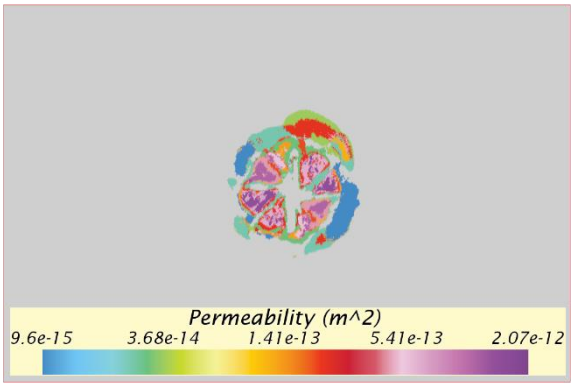


Figure 4 - Permeability map used for simulation.

The proposed and developed methodology has also been validated by recreating RIR conditions and configuration as conducted in Queens University Belfast (QUB). A simulation accuracy index is designed to quantitatively assess the accuracy of the simulation in comparison to the real injection experiment, by comparing the impacted composite reconstruction pre- and post-repair, against the results of the simulation (Figure 5 and 6). Results from 3 panels show that the simulation is at least 67% accurate, highlighting the fidelity with this reduced-order method. The reconstructions of panels provided by QUB have also been used to simulate various repair configurations in order to assess efficacy of various configuration behaviours by analysing the distribution and ratio of volume filled by resin (Figures 7 and 8). The use of optimisation is also verified and demonstrated as a proof-of-concept, with average filling improvements compared to operator-based placements of about 28%. The early form of this proposed 2D methodology has been published in ECCM20 (20th European Conference on Composite Materials) proceedings[i], and the current version is in the process of being submitted for journal publication.

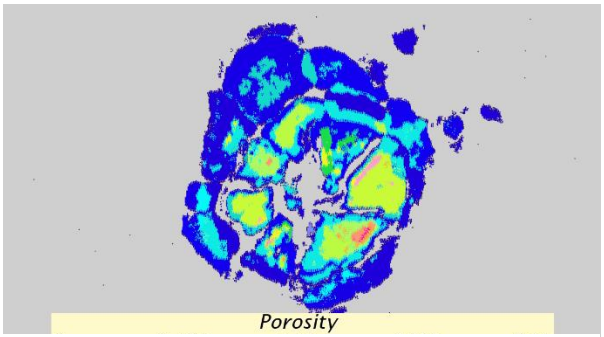


Figure 5 - Porosity map (pre-repair) of one of the validated cases.

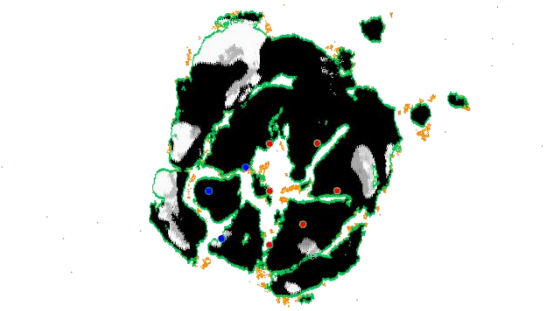

Figure 6 - Filling as observed from experimental result (by comparing pre- and post-repair porosities).

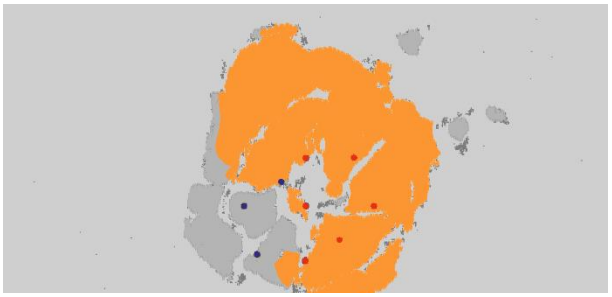

Figure 7 - Reduced-order method simulation result of the case, red and blue dots indicate injection ports and outlet vents respectively.

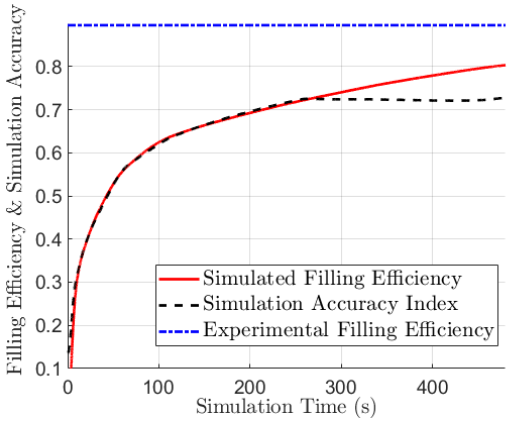


Figure 8 - The three outputs underpinning RIR modelling; the experimental filling ratio, the simulated filling ratio and the simulation accuracy index of this simulation case.

This work will directly benefit the composite industry as the proposed 2D reduced-order method uses existing and practical non-destructive evaluation techniques such as ultrasonic testing and increases the efficiency and reliability of injection repairs compared to current broad and operator experience-based guidelines.
Moreover, this project on improving RIR gives rise to many other avenues for research. Some are directly related to this work, such as increasing the sophistication of this 2D model to improve accuracy further, or related niches such as (but not limited to); developing resins tailored specifically for injection repair use, assessing and applying nanomodification of repair resins through carefully tailored nanofiller usage, or developing structural modelling methods to estimate the impact of drilling holes (for RIR) and the result of resin filling on structural properties.
The author would like to thank Dstl for the funding received for this project through the Materials for Strategic Advantage Programme.

[1] A. Asiliskender, K.Y. Lee, J. Peiró, “Reduced-Order Modelling of Composite Resin Injection Repair,” in Proceedings of the 20th European Conference on Composite Materials, June 2022.

# 9 Advanced Materials Characterization Technologies

## 9.1 Imagining Material Elasticity Using SRAS++

*Matt Clark[1*], Paul Dryburgh[2], Wenqi Li[1], Rikesh Patel[1], and Richard Smith[1]*
*[1]Optics and Photonics Group, Faculty of Engineering, University of Nottingham*
*University Park, Nottingham, NG7 2RD*
**matt.clark@nottingham.ac.uk*
*[2]Department of Surgical & Interventional Engineering, King's College London,*
*St Thomas' Hospital, Westminster Bridge Road, London SE1 7EH*

### 9.1.1 Abstract

The paper presents a new method for measuring the single-crystal elastic stiffness matrix of polycrystalline materials. This is achieved by combining a laser ultrasonic system with an inverse solver to extract both the orientation and elasticity from the SAW measurements. The solver provides accurate measurements of the single-crystal stiffness matrix of polycrystalline materials by utilizing velocity measurements for a range of propagation directions for each grain in the measurement region and performing a best fit over the orientation and elastic constant space. Results are presented for a polycrystalline nickel sample, and the measured stiffness matrix is found to be in good agreement with the values obtained from single-crystal measurements. Measuring the elastic constants of materials is important as they are vital for predicting the macroscopic mechanical behavior of the material. This is important for understanding and predicting the performance of engineering materials in real-world applications. The SRAS++ method has the potential to enable the development of new materials with tailored elastic properties, which can be optimized for specific applications, due to the relatively fast nature of the measurements.

**Keywords:** crystallographic orientation, polycrystalline microstructure, ultrasonic testing, material elastic properties

### 9.1.2 Introduction

The mechanical properties of materials are critical for their performance in real-world applications. Understanding these properties is essential for designing and engineering materials that can withstand the stresses and strains of everyday use. One of the most important mechanical properties of materials is their elastic stiffness, which describes how much a material will deform under a given load [1]. In this paper, we present a new method for measuring the single-crystal elastic stiffness matrix of polycrystalline materials.

The technique builds on the capabilities of spatially resolved acoustic spectroscopy (SRAS), a laser ultrasound technique for measuring the surface acoustic wave velocity of a material [2]. SRAS uses a pulsed infrared laser to illuminate the sample with a grating pattern of light. The period of the grating determines the acoustic wavelength, this combined with the acoustic properties of the material, determines the frequency of the generated ultrasound. Measuring the SAW as it propagates away from the

generation region with a continuous wave laser allows the frequency ($f$) to be measured. Combining this with the known wavelength information ($\lambda$) allows the SAW velocity ($v$) to be calculated via $v = f \lambda$. As this doesn't rely on the time of flight the measurement is robust and easy to obtain.

The SAW phase velocity depends on the elastic properties and the crystallographic orientation of the material. If the orientation changes then the velocity can change significantly. In its simplest form this allows contrast of grains to be imaged for polycrystalline materials [3]. Combining measurements from multiple acoustic propagation directions with the elastic constants for the material, typically obtained from the literature, it is possible to determine the crystal orientation of the grains [4]. This technique been used for inspecting many engineering materials such as titanium, nickel, steel, aluminum and silicon [5, 6, 7].

This paper details recent work to enable the determination of, or the refinement of the elastic constants for measurements on polycrystalline materials. The paper is laid out in the following order, we firstly discuss the engineering impact of this work, and then the methodology used, the results obtained, and conclude by summarizing the significance of this research.

### 9.1.3 Engineering Impact

Measuring the single-crystal elastic stiffness matrix of polycrystalline materials has important engineering applications. This information is critical for predicting the macroscopic mechanical behavior of materials and designing new materials with tailored mechanical properties. For example, the development of high-strength, lightweight materials for aerospace and automotive applications requires a deep understanding of the mechanical behavior of materials. By accurately measuring the single-crystal elastic stiffness matrix of polycrystalline materials, it is possible to design materials with optimized elastic properties, such as high strength and low weight.

### 9.1.4 Methodology

The proposed method for measuring the single-crystal elastic stiffness matrix of polycrystalline materials combines a laser ultrasonic system with an inverse solver to extract both the orientation and elasticity from the SAW measurements. Spatially resolved acoustic spectroscopy is used to measure the SAW velocities of the material for a number of wave propagation directions. The SRAS instrument used a wavelength of 24 microns, and a generation image size of 200 microns, giving a spatial resolution of 100 microns. Single shot measurements were used to take velocity images for 18 different propagation directions (0:10:170 degrees).

Figure 1 demonstrates this process. A polycrystalline specimen (a) is measured to produce velocity surfaces for each grain (b), these are fed into the inverse solver, where they are compared to the database of velocity surfaces calculated from the forward model (c) for all crystal orientations and for all elastic constants chosen. For details of the forward model see [4, 8]. By determining the best fit (d) across all grains both the

individual grain orientations (e) and the shared optimal single crystal elastic constants can be determined (f).

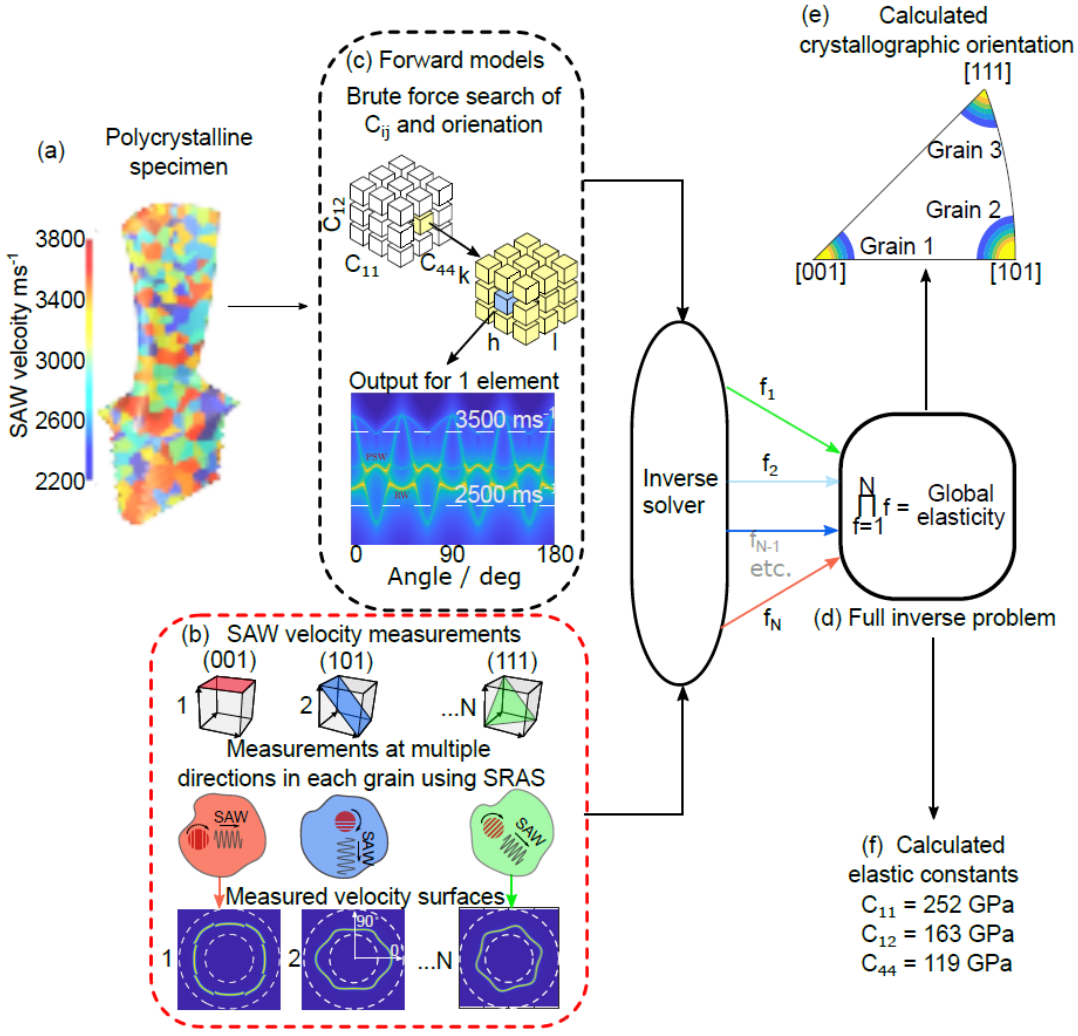


Figure 1 - The new inversion method described in this work, detailing the process of calculating the crystallographic orientation and elastic constants for a synthetic specimen. (a) The SAW velocity is measured in multiple grains using spatially resolved acoustic spectroscopy. By rotating the generation patch velocity surfaces can then be built up for each grain. The velocity surfaces shown are from three arbitrary planes of nickel (here we use three primary planes as examples). (c) The forward model is searched for the range of possible elastic constants (C11;C12;C44) and crystalline orientation (hkl). Each element of the forward model determines the velocity of all SAWs which can propagate across that plane. (d) The output of the forward model search and one experimentally measured velocity surface are input to the inverse solver. The inverse solver calculates the `goodness of fit' between the velocity surface and each element of the forward model. This is then repeated for each measured grain before taking the product of the figure of merit for all grains. The specimens' elastic constants are then determined by the location of the maxima. (e) Calculated crystallographic orientation from the inverse solver, showing the three grains on one pole figure. (f) Final calculated elastic constants for this specimen.

### 9.1.5 Results

A CMSX-4 sample was measured with SRAS. If the literature elastic constants are used to determine the optimal orientation of each of the grains Fig. 2(a) the values found do not match those from EBSD Fig.2 (c). If the SRAS++ method is used to determine both

the single crystal elastic constants and the individual grain orientations then the result is significantly improved. Fig 2.(b). Now the individual grain orientations match those expected from EBSD.

The determined elastic constants are $C_{11}$ = 251.5 GPa, $C_{12}$ = 163 GPa and $C_{44}$ = 119 GPa [9], which differ from the literature values of $C_{11}$ = 251 GPa, $C_{12}$ = 159 GPa and $C_{44}$ = 132 GPa. This particular sample had undergone heat treatment and this process has clearly modified the elastic properties of the sample.

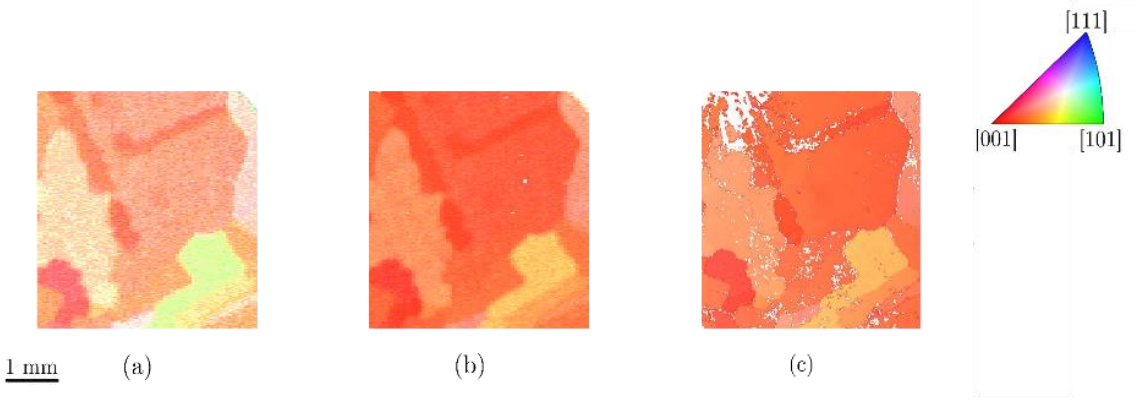


Figure 2 - Compares the inverse pole figures for the CMSX-4 specimen, from (left to right) SRAS using existing elastic from literature (a), SRAS using inversion elastic constants (b) and EBSD (c) [6]. The elastic constants calculated by the SRAS inversion in this work have significantly improved the orientation result, relative to the EBSD dataset.

### 9.1.6 Conclusion

SRAS++ provides a way to obtain the elastic properties of materials in a rapid and non-destructive way. The ability of the solver to extract elastic constants $C_{ij}$ without a-prioir knowledge of the crystallographic orientation comes from solving $C_{ij}$ globally for a multitude of (initially) unknown crystal orientations. Future integration of the instrument in advance material manufacturing environments will allow near real-time measurement of the elastic properties. This will allow the rapid exploration of new materials with tailored mechanical properties across a wide range of applications.

### References

[1] M. H. Sadd, Elasticity: theory, applications, and numerics, Academic Press, 2009.

[2] R. J. Smith, W. Li, J. Coulson, M. Clark, S. D. Sharples, M. G. Somekh, Spatially resolved acoustic spectroscopy for rapid imaging of material microstructure and grain orientation, Measurement Science and Technology 25 (2014) 1-11. doi:10.1088/0957-0233/25/5/055902.

[3] S. D. Sharples, M. Clark, M. G. Somekh, Spatially resolved acoustic spectroscopy for fast noncontact imaging of material microstructure, Opt. Express 14 (2006) 10435 - 10440. doi:10. 1364/oe.14.010435.

[4] W. Li, S. D. Sharples, R. J. Smith, M. Clark, M. G. Somekh, Determination of crystallographic orientation of large grain metals with surface acoustic waves, Journal of the Acoustical Society of America 132 (2012) 738 -745. doi:10.1121/1.4731226.

[5] W. Li, J. Coulson, J. W. Aveson, R. J. Smith, M. Clark, M. G. Somekh, S. D. Sharples, Orientation characterisation of aerospace materials by spatially resolved acoustic spectroscopy, Journal of Physics: Conference Series 520 (2014) 1 - 4. doi:10.1088/1742-6596/520/1/012017.
[6] R. Patel, W. Li, R. J. Smith, S. D. Sharples, M. Clark, Orientation imaging of macro-sized polysilicon grains on wafers using spatially resolved acoustic spectroscopy, Scripta Materialia 140 (2017) 67 - 70. doi:10.1016/j.scriptamat.2017.07.003.
[7] P. Dryburgh, R. J. Smith, P. Marrow, S. J. Lainé, S. D. Sharples, M. Clark, W. Li, Determining the crystallographic orientation of hexagonal crystal structure materials with surface acoustic wave velocity measurements, Ultrasonics, Vol. 108, 2020, 106171. doi:10.1016/j.ultras.2020.106171.
[8] Paul Dryburgh, Wenqi Li, Don Pieris, Rafael Fuentes-Domínguez, Rikesh Patel, Richard J. Smith, Matt Clark, Measurement of the single crystal elasticity matrix of polycrystalline materials, Acta Materialia, Vol. 225, 2022, 117551. doi:10.1016/j.actamat.2021.117551.
[9] X. Zhang, P. R. Stoddart, J. D. Comins, A. G. Every, High-temperature elastic properties of a nickel-based superalloy studied by surface Brillouin scattering, Journal of Physics: Condensed Matter 13 (2001) 2281{2294. doi:10.1088/0953-8984/13/10/320.

## 9.2 What can we *SRAS*? – Towards in-situ rough surface microstructure inspection

Rikesh Patel[1*], Wenqi Li[1], Paul Dryburgh[2], Don Pieris[3], Rafael Fuentes-Dominguez[1], Richard Smith[1], and Matt Clark[1]

[1]Optics and Photonics Group, Faculty of Engineering, University of Nottingham
University Park, Nottingham, NG7 2RD
*rikesh.patel@nottingham.ac.uk
[2]Department of Surgical & Interventional Engineering, King's College London,
St Thomas' Hospital, Westminster Bridge Road, London SE1 7EH
[3]Electronic and Electrical Engineering, University of Strathclyde,
James Weir Building, Montrose St, Glasgow G1 1XQ

### 9.2.1 Abstract

Spatially resolved acoustic spectroscopy (SRAS) is a laser ultrasonic material characterisation technique that is able to image crystallographic contrast maps as well as crystallographic orientation (SRAS+). More recently, a novel method has been developed to extract the elasticity matrix itself of existing and new materials (SRAS++). However, the characterisation of materials has been limited to the laboratory environment and on prepared samples.
This paper presents the development of a SRAS instrument for use on optically rough materials, as they are manufactured or fabricated, using a commercially available random-quadrature interferometer. The novel method developed enables the possibility of in-field and in-situ interrogation of samples with difficult geometries or parts that are difficult practically to remove and prepare, making it particularly useful for immediate part integrity and performance metrics. The measured results from a selection of samples with known surface conditions is presented, and we conclude on the viability of the detection regime for a SRAS instrument.

**Keywords:** material characterisation, grain contrast measurements, rough surface laser ultrasonics

### 9.2.2 Background

Material microstructure refers to the characteristics of grains within a material – aspects such as crystal size, location, and orientation are all affected by production factors such as processing, heat treatment, and deformation. Measuring the microstructure of engineering alloys is crucial for determining mechanical properties, as well as their response to external stimuli. In particular, the orientation of grains within the material can greatly affect its properties as many materials exhibit anisotropic behaviour, where their properties vary depending on the direction of reference. Microstructure optimisation of mission and safety critical components is key in high-value engineering industries, and microstructure imaging is the major tool in facilitating this.

Mapping the material microstructure during part manufacturing is beneficial for several reasons. Firstly, it enables the identification of any inconsistencies or defects in the material, which can help to prevent the failure of the final part. Secondly, it allows for the optimisation of the manufacturing process by identifying areas of the part that may require additional processing to achieve the desired properties. Additionally, it provides valuable information for quality control and assurance, ensuring that the final product meets required standards. Finally, mapping the microstructure of a part can help to improve the overall understanding of the material and how it behaves under different conditions, which can inform future manufacturing processes and material designs.
Current imaging of microstructure is performed offline – with grain contrast imaging utilising various etching techniques or polarised light micrography. More resource intensive techniques such as electron backscatter diffraction (EBSD) and X-ray diffraction (XRD) can also extract crystallographic orientation to high accuracy. However, these techniques require some degree of sample destruction or incur a large time cost for operation, and given the limitation of these few techniques, none are practically useful outside of a laboratory setting. Statistical microstructure models are often developed given a particular production protocol, however the attained precision in any model for a produced part would not be sufficient for the very industries that require microstructure information.
Spatially resolved acoustic spectroscopy (SRAS) is a laser ultrasonic material characterisation technique – the system is all-optical (i.e. non-contact), where a controlled surface acoustic wave (SAW) packet is thermo-elastically generated by a grating patterned incident pulsed laser. The wave packet contains a frequency that does not change as it propagates across the material and is dependent only on the wave velocity at the point of generation. This results in a robust measurement of the wave packet frequency (and therefore SAW velocity) at generation, as it can be made at any point after generation. The measurement is unaffected by the microstructure along the medium and simultaneously reveals the properties at a single point on the material. Translation of multiple SAW measurements allows for rapid imaging of grain contrast (SRAS)[1], which can be utilised alongside material elastic properties (from literature) to map crystallographic orientation (SRAS+)[2], and we can go even further beyond to identify the material elastic properties themselves (SRAS++)[3].

In order to detect the generated acoustic wave, optical beam deflection method is used – a second continuous wave laser incident on the measured material experiences a slight change in the reflection angle (with respect to the optical axis) as the generated SAW perturbs the surface during propagation. This slight movement can simply be detected across two adjacent photodiode output in differential (i.e. a split photodiode in 'knife-edge' configuration) if the surface is optically smooth, where the beam profile remains unchanged on return. One limiting factor in determining the mapped acoustic image resolution is determined by the operational bandwidth of the detector device, where, for example a 1GHz device could theoretically be used to image with a resolution of ~15um on titanium (given a 5-fringe grating pattern). However, this detection method no longer works if the interrogated surface is rough, as the return light would consist of speckles.

Recent advancements in laser ultrasound rough surface detection technology have made it possible to use the SRAS technique on as-fabricated, as-deposited or machined surfaces, meaning it can become truly non-destructive as no surface preparation is required. The advantage of an inspection system with unrestricted interrogation limits means that a system could be built to operate in-situ of a workshop or fabrication environment. Interferometric detector systems that perform multichannel random-quadrature demodulation have been developed over the past two decades to extract ultrasound signals off real surfaces [4] – the latest Quartet model developed by Sound-n-Bright can detect out-of-plane motion with a high operational bandwidth of 100MHz. This study investigates the capabilities a SRAS system integrated with such a rough surface detector to examine the viability of scanning samples with defined rough surface conditions.

### 9.2.3 Methodology and results

The surface condition of engineering alloys, and subsequent manufactured parts, vary with the processes that are applied to the base material – this could include variations in heat treatment or fabrication temperature, material feed rates, machining speeds and tool wear, as well the material chemistry and properties themselves. It would be difficult to definitively suggest that a useful signal could be obtained off a rough surface using the outline technique and detection equipment, as there are a number of other factors from instrumentation alignment to sample reflectivity that could affect detection. However, there are a number of metrics that can be used to quantify the surface profile of manufactured parts that could give an indication of whether the rough surface SRAS system could work on such a surface – the often-quoted parameter $R_a$ describes the average deviation of surface height from its mean, and consequently the higher the $R_a$ value, the 'rougher' the surface. Given different manufacturing finishes, processes, and technologies, it is entirely possible to have similar $R_a$ values but with differing overall form.

Roughness comparison specimens are often used in place of expensive profilometers when rapid gauging of a surface condition from a process is required – they are created using different common machining methods (e.g. grinding, lapping, etc.) and have been profiled by the manufacturers. For this study, nine different nickel comparator specimens were obtained from Rubert + Co Ltd and GAR Electroforming. Figure 1 shows one of the

nine comparators used, where spark erosion has created different surface roughnesses – the $R_a$ value is indicated on the comparator (top). The Quartet equipped SRAS system was used to scan each sub-specimen – a small subregion of each scan is shown in Figure 1 inset in the bottom left of each sub-specimen. The grain sizes in the electroformed specimens are smaller than can be resolved using this version of SRAS, so the prominent acoustic velocity within the detection area is measured – the colour in the maps shows the measured point velocity.

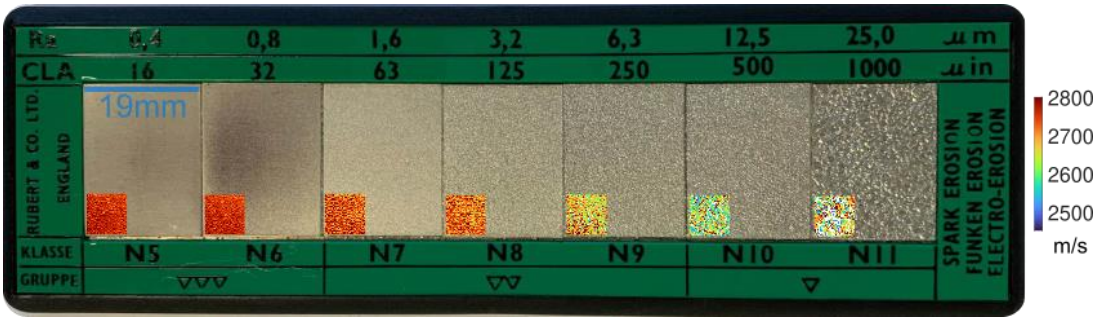


Figure 1 **-** Photograph of one of the roughness comparator specimens with increasing roughness (labelled top) from left to right (created using spark erosion). Inset images in the bottom-left of each sub-specimen shows the SRAS scan in that area, with the colour indicating the measured acoustic velocity (colour bar on right). Points where a white colour is used indicates data dropout.

The variation of the velocity across the entire specimen is due to the change in roughness rather than the change in material microstructure [5]. To determine the viability of using SRAS on different surface finishes and roughness values, the average Signal-Noise Ratio (SNR) of the acoustic measurements across the sample can be used. Additionally, the data dropout rate (the number of points where the returned light intensity on the detector is insufficient for measurement) can also be used – in the acoustic velocity map insets, these points are shown in white. Table 1 shows these values across all nine comparator specimens, where roughness was created through (left-right) honing, grinding, lapping, shot blasting, grit blasting, turning, horizontal milling, vertical milling and spark erosion. The green columns in the table shows the average SNR across the sample, where each point was measured single shot (i.e. no acquisition averaging was used), and the blue column shows the SRAS data dropout rate (in percent) for each sub-specimen - blank cells show no sub-specimen was available for the indicated roughness.

Table 1 - Table showing the nine different roughness comparator specimens (top) and the roughness in Ra of each of their sub-specimens (left). Values in the blue columns show the percentage of points where data could not be collected, values in the green column show the average Signal-Noise ratio of the points on the

sub-specimens where data could be collected – for all measurements, no averaging was used during acquisition.

| Finish | Honing | | Grinding | | Lapping | | Shot blasting | | Grit blasting | | Turning | | Horz. milling | | Vert. milling | | Spark erosion | |
|---|---|---|---|---|---|---|---|---|---|---|---|---|---|---|---|---|---|---|
| *Ra (μm)* | Scan Signal-Noise Ratio (dB) - no averaging | | | | | | | | | | | | | | | | | |
| *0.05* | 23.7 | 35 | 21.7 | 0 | 25.7 | 0 | - | - | - | - | - | - | - | - | - | - | - | - |
| *0.1* | 23.2 | 41 | 19.5 | 1 | 24.8 | 1 | - | - | - | - | - | - | - | - | - | - | - | - |
| *0.2* | 24.9 | 38 | 21.4 | 1 | 24.5 | 1 | - | - | - | - | - | - | - | - | - | - | - | - |
| *0.4* | 23.7 | 35 | 23.5 | 0 | - | - | 21.9 | 0 | 22.6 | 0 | 21 | 57 | 24.4 | 1 | 24.2 | 1 | 21.9 | 0 |
| *0.8* | 21.9 | 41 | 23.6 | 1 | - | - | 17.5 | 5 | 19.5 | 5 | 24.9 | 21 | 23.2 | 2 | 25.8 | 1 | 18.5 | 1 |
| *1.6* | 21.7 | 45 | 27.3 | 2 | - | - | 18.7 | 5 | 13.9 | 10 | 23.1 | 21 | 17.4 | 20 | 21.9 | 0 | 13.9 | 2 |
| *3.2* | - | - | - | - | - | - | 12.5 | 17 | 10.2 | 16 | 22.5 | 27 | 20.6 | 6 | 24.9 | 2 | 13.2 | 2 |
| *6.4* | - | - | - | - | - | - | 13.7 | 13 | 8.8 | 26 | 19 | 45 | 24.7 | 3 | 21.1 | 13 | 14.7 | 13 |
| *12.5* | - | - | - | - | - | - | 16.4 | 23 | 10.8 | 41 | 14 | 59 | 25.9 | 3 | 23.7 | 4 | 14 | 30 |
| *25* | - | - | - | - | - | - | - | - | - | - | - | - | - | - | - | - | 16.1 | 38 |
| | Data dropout rate (%) | | | | | | | | | | | | | | | | | |

The general SNR of this rough surface SRAS system is about 20dB, with full data coverage possibly when these nickel specimens have low roughness. With increasing values of $R_a$, a lower SNR and higher dropout rates results (although this is not always the case at the highest $R_a$ values). However, this is variable depending on the resultant form given by the different mechanical surface finishes – the dropout rate is particularly variable for honing and turning results, where these rates are much worse than their counterpart specimens and do not necessarily increase with $R_a$. This is most likely due to these specimens containing regular patterns in the surface causing intervals where little light reaches the detector. As an example, if the input signal has an SNR of 15dB, this would equate to a measurement wave velocity standard deviation of ~35m/s (for imaging).

### 9.2.4 Discussion

As manufacturing processes become more refined, surface roughnesses and physical flaws are reduced – this is particularly critical for powder bed fusion additive manufacturing, where a correlation has been seen between surface roughness and internal defects[6]. For the near future however, it is unlikely that practical manufacturing and fabrication will produce parts that are considered optically smooth (e.g. $R_a < 50$nm). SRAS systems up until now suffered from two major disadvantages – the spatial resolution of the microstructure is about $10^5$ times worse when compared with EBSD, and it can only image off optically smooth surfaces. This paper describes a method to remedy this latter issue through integration with a commercially available interferometer detector. To illustrate the capability of this new arrangement, measurements were made on samples with predefined roughnesses where we have shown velocity images on a selection of specimens, and described the data dropout rate and average SNR.

Answering the question “What can we SRAS?” is an open-ended question as it depends on a number of factors – in this paper, we have given an indication of what possible surface roughness conditions we are able to get a useful signal off. Data dropouts in the samples presented are chiefly caused by a loss of detection light – there are mitigations that can be put into place to improve this such as adjusting the optical alignment and rescanning a sample (at a cost of interrogation speed), increasing the number of detector units (at a monetary and space cost), or broadening the detection area on the surface (which will reduce the produced image resolution). Surface roughness itself is a

complex issue and this study has only considered samples that are locally rough, where the absolute mean gradient of the $R_a$ value is comparable with the $R_a$ value itself – for specimens with similar $R_a$ but a high degree of waviness (where the absolute mean gradient is much lower than the $R_a$) as seen with direct energy deposition additive manufactured parts, the optical return is likely to form fewer speckles but could entirely miss the detection system altogether. For different manufacturing environments, it is likely different arrangements with these detectors would need to be designed.

## References


(1) Sharples, Steve D. et al. 2006. 'Spatially Resolved Acoustic Spectroscopy for Fast Noncontact Imaging of Material Microstructure'. Optics Express 14(22): 10435.

(2) Li, Wenqi et al. 2012. 'Determination of Crystallographic Orientation of Large Grain Metals with Surface Acoustic Waves'. The Journal of the Acoustical Society of America 132(2): 738–45.

(3) Dryburgh, Paul et al. 2022. 'Measurement of the Single Crystal Elasticity Matrix of Polycrystalline Materials'. Acta Materialia 225: 117551.

(4) Blum, T. et al. 2008. 'Non-Destructive Testing Using Multi-Channel Random-Quadrature Interferometer'. In AIP Conference Proceedings, Golden (Colorado): AIP, 239–46.

(5) Sarris, Georgios et al. 2021. 'Attenuation of Rayleigh Waves Due to Surface Roughness'. The Journal of the Acoustical Society of America 149(6): 4298–4308.

(6) Yonehara, Makiko et al. 2021. 'Correlation between Surface Texture and Internal Defects in Laser Powder-Bed Fusion Additive Manufacturing'. Scientific Reports 11(1): 22874.

## Initial distribution

| | | |
|---|---|---|
| 1. | Dstl KIS Athena | electronic |
| 2. | Contributors | electronic |
| 3. | ICAF National Delegates | electronic |

## Report documentation page v5.0

* Denotes a mandatory field

| | | | | | |
|---|---|---|---|---|---|
| **1a.** | **Report number: *** | DSTL/TR150228 | **1b.** | **Version number:** | v1 |
| **2.** | **Date of publication: *** | 21/06/2023 | **3.** | **Number of pages:** | 66 |
| **4a.** | **Report UK protective marking: *** | UK OFFICIAL | | | |
| **4b.** | **Report national caveats: *** | NONE | | | |
| **4c.** | **Report descriptor: *** | NONE | | | |
| **5a.** | **Title: *** Review of aeronautical fatigue and structural integrity investigations in the UK during the period May 2021 - April 2023 | | | | |
| **5b.** | **Title UK protective marking: *** | UK OFFICIAL | | | |
| **5c.** | **Title national caveats: *** | NONE | | | |
| **5d.** | **Title descriptor: *** | NONE | | | |
| **6.** | **Authors: *** Hallam David A | | | | |
| **7a.** | **Abstract: *** This review is a summary of the aeronautical fatigue and structural integrity investigations carried out in the United Kingdom during the period May 2021 to April 2023. The review has been compiled for the 38th Conference and 31st Symposium of the International Committee on Aeronautical Fatigue and Structural Integrity (ICAF) on 26th – 29th June 2023 in Delft, The Netherlands and will be archived on the ICAF website https://www.icaf.aero/. Contributions generously provided by colleagues from within the aerospace industry and universities are gratefully acknowledged. The names of contributors and their affiliation are shown below the title of each item. | | | | |
| **7b.** | **Abstract UK protective marking: *** | UK OFFICIAL | | | |
| **7c.** | **Abstract national caveats: *** | NONE | | | |
| **7d.** | **Abstract descriptor: *** | NONE | | | |
| **8.** | **Keywords:** Aeronautical fatigue, Structural integrity, ICAF | | | | |

Please note: Unclassified, Restricted and Confidential markings can only be used where the report is prepared on behalf of an international defence organisation and the appropriate prefix (e.g. NATO) included in the marking.

* Denotes a mandatory field

| | |
|---|---|
| **9. Name and address of publisher: *** <br><br> Dstl <br> Porton Down <br> Salisbury <br> Wiltshire <br> SP4 0JQ | **10. Name and address of funding source:** |
| **11. Funding source contract:** | |
| **12. Dstl project number:** | |
| **13. Programme:** | |
| **14. Other report numbers:** | |
| **15a. Contract start date:** | **15b. Contract end date:** |
| **16. IP conditions for report: *** Non-MOD funded Dstl authored report | |
| **17a. Patents:** NO | |
| **17b. Application number:** | |
| **18. Release authority role:** | |

Guidance on completing the report documentation page can be found on the Gov.UK website.